

ARTICLE

# Computational analyses reveal spatial relationships between nuclear pore complexes and specific lamins

Mark Kittisopikul<sup>1,2\*</sup>, Takeshi Shimi<sup>1,3\*</sup>, Meltem Tatli<sup>4</sup>, Joseph Riley Tran<sup>5</sup>, Yixian Zheng<sup>5</sup>, Ohad Medalia<sup>4</sup>, Khuloud Jaqaman<sup>2,6</sup>, Stephen A. Adam<sup>1</sup>, and Robert D. Goldman<sup>1</sup>

**Nuclear lamin isoforms form fibrous meshworks associated with nuclear pore complexes (NPCs). Using datasets prepared from subpixel and segmentation analyses of 3D-structured illumination microscopy images of WT and lamin isoform knockout mouse embryo fibroblasts, we determined with high precision the spatial association of NPCs with specific lamin isoform fibers. These relationships are retained in the enlarged lamin meshworks of *Lmna*<sup>-/-</sup> and *Lmnb1*<sup>-/-</sup> fibroblast nuclei. Cryo-ET observations reveal that the lamin filaments composing the fibers contact the nucleoplasmic ring of NPCs. Knockdown of the ring-associated nucleoporin ELYS induces NPC clusters that exclude lamin A/C fibers but include LB1 and LB2 fibers. Knockdown of the nucleoporin TPR or NUP153 alters the arrangement of lamin fibers and NPCs. Evidence that the number of NPCs is regulated by specific lamin isoforms is presented. Overall the results demonstrate that lamin isoforms and nucleoporins act together to maintain the normal organization of lamin meshworks and NPCs within the nuclear envelope.**

## Introduction

The nuclear envelope (NE) is a complex multicomponent structure separating the nuclear genome from the cytoplasm. It has evolved as a highly compartmentalized multifunctional organelle with a wide range of functions. The NE structure includes the nuclear lamina (NL), a double membrane bilayer forming a lumen continuous with the endoplasmic reticulum and nuclear pore complexes (NPCs). However, details of the structural and spatial relationships among the components of the NE have been difficult to define. This lack of information is largely attributable to the dense packing and close spatial relationships of the structures comprising the NE (Aebi et al., 1986; Fisher et al., 1986; Goldman et al., 1986; McKeon et al., 1986). To better understand the structural relationships within the NE, we have combined super-resolution light microscopy with recently developed computer vision techniques. This approach has allowed us to quantitatively analyze the structural organization of the lamins and NPCs in the NE by making precise measurements of lamin structures and NPC localization over large areas of the NE. Our goal is to test the utility of large datasets to provide new insights into the interactions between these two major components of the NE.

The four major lamin isoforms in somatic cells are lamin A (LA), lamin C (LC), lamin B1 (LB1), and lamin B2 (LB2). LA and LC are alternative splicing isoforms encoded by the *Lmna* gene, LB1 is encoded by the *Lmnb1* gene, and LB2 is encoded by the *Lmnb2* gene. These type V intermediate filament proteins are closely apposed to the inner nuclear membrane where they assemble into discrete fibrous meshworks. In mouse embryo fibroblast (MEF) nuclei, the NL is a 13.5-nm-thick layer composed of 3.5-nm-diameter filaments (Turgay et al., 2017). Using 3D-structured illumination microscopy (3D-SIM) combined with computer vision analysis, we demonstrated that bundles of these filaments, termed fibers in the light microscope, are nonrandomly organized into complex interwoven meshworks within the NL (Shimi et al., 2015; Turgay et al., 2017). Notably, each lamin isoform assembles into distinct meshworks with similar structural organization (Shimi et al., 2015). Previous studies on *Lmna*<sup>-/-</sup> MEFs (Sullivan et al., 1999) showed that loss of LA/LC caused dramatic changes in nuclear morphology with some NPC clustering. Subsequently, we showed that the meshworks formed by individual lamin isoform fibers are significantly expanded in size in *Lmna* or *Lmnb1* knockout (KO)

<sup>1</sup>Department of Cell and Developmental Biology, Feinberg School of Medicine, Northwestern University, Chicago, IL; <sup>2</sup>Department of Biophysics, University of Texas Southwestern Medical Center, Dallas, TX; <sup>3</sup>Cell Biology Center and World Research Hub Initiative, Institute of Innovative Research, Tokyo Institute of Technology, Yokohama, Japan; <sup>4</sup>Department of Biochemistry, University of Zurich, Zurich, Switzerland; <sup>5</sup>Department of Embryology, Carnegie Institution for Science, Baltimore, MD; <sup>6</sup>Lyda Hill Department of Bioinformatics, University of Texas Southwestern Medical Center, Dallas, TX.

\*M Kittisopikul and T. Shimi contributed equally to this paper; Correspondence to Robert D. Goldman: [r-goldman@northwestern.edu](mailto:r-goldman@northwestern.edu); M. Kittisopikul's present address is Janelia Research Campus, Howard Hughes Medical Institute, Ashburn, VA; T. Shimi's present address is Institute of Innovative Research Advanced Research Center for Cell Biology, Tokyo Institute of Technology, Yokohama, Kanagawa, Japan.

© 2021 Kittisopikul et al. This article is distributed under the terms of an Attribution–Noncommercial–Share Alike–No Mirror Sites license for the first six months after the publication date (see <http://www.rupress.org/terms/>). After six months it is available under a Creative Commons License (Attribution–Noncommercial–Share Alike 4.0 International license, as described at <https://creativecommons.org/licenses/by-nc-sa/4.0/>).

MEF nuclei compared with the lamin meshworks in WT or *Lmnb2* KO MEF nuclei, demonstrating that LA/LC and LBI interactions are required for normal lamin fiber meshwork structure in WT MEFs (Shimi et al., 2015).

The NPCs penetrate the NE, forming transport passageways delineated by the fusion of the inner and outer nuclear membranes, thereby allowing for bidirectional transport across the NE. They are composed of multiple copies of 30 proteins known as nucleoporins (Beck and Hurt, 2017). For many years, it has been apparent that there are structural interactions between the NL and NPCs of vertebrate nuclei. The earliest studies on identification of components of the NE identified a cell-free NPC-NL fraction that could be isolated under fairly stringent conditions, suggesting their strong physical association (Kay et al., 1972; Dwyer and Blobel, 1976; Scheer et al., 1976; Aebi et al., 1986). In addition, both lamins and the NPCs are relatively immobile in the plane of the NE, indicating that both are anchored in some fashion (Broers et al., 1999; Moir et al., 2000; Rabut et al., 2004). Both the nuclear lamins and NPC structures are closely associated with chromatin at the nuclear periphery (Guelen et al., 2008; Peric-Hupkes et al., 2010; Ibarra and Hetzer, 2015), with the NPCs located in spaces where both the lamina and heterochromatin appear to be discontinuous (Fawcett, 1966; Ou et al., 2017). Super-resolution microscopy analysis of lamins and NPCs in *Lmna*<sup>-/-</sup> fibroblasts also found NPCs closely associated with exogenously expressed LA and LC in Xie et al. (2016), where an mEOS fluorescent protein tag was used in some experiments. Some clustering of NPCs within the remaining LBI networks has also been reported in *Lmna*<sup>-/-</sup> fibroblasts (Xie et al., 2016). Prior studies by cryo-electron tomography (cryo-ET) also support the close association of lamin filaments with the NPCs (Mahamid et al., 2016; Turgay et al., 2017; Tatti and Medalia, 2018).

Biochemical analyses of lamin-NPC interactions have shown connections between lamins and a subset of specific nucleoporins (Hase and Cordes, 2003; Krull et al., 2004; Al-Haboubi et al., 2011). More recently, proximity-dependent biotin identification, BioID, recognized several lamin-associated nucleoporins including NUP153, ELYS, and TPR (Roux et al., 2012; Xie et al., 2016). These nucleoporins localize to the nucleoplasmic aspect of NPCs, which lie in close proximity to the NL (Walther, 2001; Rasala et al., 2008). The distribution of NPCs is nonrandom, with characteristic center to center spacing varying according to species ranging from human to frog (Maul, 1977). Furthermore, removal of all lamins from MEFs or mESC-derived fibroblast-like cells leads to clustering of the NPCs, which can be rescued by reexpression of either A- or B-type lamins (Guo and Zheng, 2015). These observations suggest that lamins play an important role in regulating the distribution of NPCs.

Although the extant evidence strongly suggests that lamins interact with nucleoporins to anchor the NPCs in the NE, how each lamin isoform contributes to these interactions remains unknown. In this study, we investigate the structural relationships between each lamin isoform fiber meshwork and NPCs over large areas of the NE at nanoscale precision using 3D-SIM with newly developed computational procedures for subpixel quantitative image analysis. The analysis involves collecting

positional information derived from large numbers of individual NPCs and determining their spatial relationship to each lamin isoform fiber comprising the NL meshworks. This quantitative approach is necessitated by the complexity of the four lamin fiber meshworks and NPCs located within a thin layer at the nuclear surface. The results of our analyses demonstrate that NPCs are closely associated with lamin fibers. At higher resolution, cryo-ET confirms that both LA/LC and LBI filaments interact closely with the NPCs at the nucleoplasmic ring. Targeted disruption of nucleoporins and lamin isoforms demonstrates the interdependence of the spatial distributions of lamin fibers and NPCs.

## Results

### NPCs are structurally linked to lamin fibers

We used 3D-SIM and image reconstruction to determine the structural relationships among immunolabeled lamin fiber meshworks and NPCs in MEFs. NPCs in WT MEFs were distributed all across the NL region but did not show an obvious colocalization with any of the lamin meshworks, as indicated by the very few white areas in merged overlays (Fig. 1 A). This was remarkable because some colocalization of lamins and NPCs would be expected by chance given the densely packed environment of the NL. This lack of colocalization between lamins and NPCs suggested the existence of a bona fide spatial relationship. We took advantage of our previous finding that the spaces or “faces” delineated by lamin fibers comprising the meshworks increase in size in *Lmna*<sup>-/-</sup> and *Lmnb1*<sup>-/-</sup> MEF nuclei (Shimi et al., 2015). This allowed us to examine the association between NPCs and specific lamin isoforms in WT, *Lmna*<sup>-/-</sup>, and *Lmnb1*<sup>-/-</sup> MEFs. Importantly, NPCs remained in close proximity to the LA and LBI fibers in the expanded meshworks of *Lmna*<sup>-/-</sup> and *Lmnb1*<sup>-/-</sup> MEF nuclei, respectively, and were absent in the meshwork faces (Fig. 1 B). These results strongly suggest that LA and LBI are required for the normal distribution of NPCs. Although these images provide qualitative evidence that there is an association between lamin isoform fibers and NPCs, it is important to verify such associations using a quantitative approach to ascertain the extent of the relationships between each lamin isoform fiber and NPCs.

### Image analysis reveals enrichment of NPCs within 30–100 nm of LA fibers in WT and *Lmnb1*<sup>-/-</sup> MEFs

We developed quantitative image analysis tools to precisely determine the spatial relationships between lamin isoform fibers and NPCs and to localize both structures with subpixel precision in dense and sparse lamin meshworks (Fig. 2 A; details of analysis tools in Materials and methods). We reasoned that by measuring the distances between the centers of lamin fibers and the center of lamin meshwork faces to the centers of NPCs (Fig. S1), we could quantitatively assess the association of NPCs with individual lamin isoforms. To evaluate the frequency of observing distances between the lamin fibers or face centers and NPCs by chance, we compared our observed distance measurements with the expected distances under a null hypothesis, which assumes the NPCs and lamin meshworks have

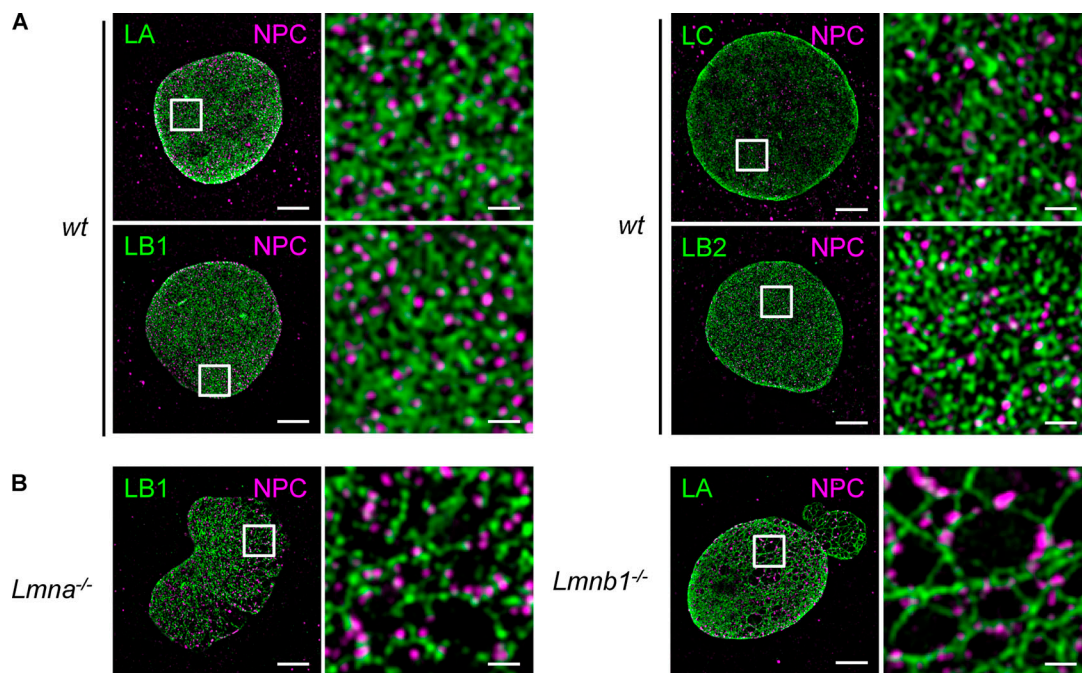


**Figure 1. NPCs are arranged along LA and LB1 fibers in enlarged lamin meshworks. (A and B)** Colabeling of lamins and NPCs in WT and lamin KO MEF nuclei using indirect immunofluorescence with a pair of specific antibodies against each lamin isoform (LA, LB1, LB2, or LC) and the FXFG-repeat nucleoporins. **(A)** WT MEF nuclei colabeled with the indicated lamin isoform and FXFG-repeated nucleoporins. **(B)** Nuclei of *Lmna*<sup>-/-</sup> (left pair) and *Lmnb1*<sup>-/-</sup> (right pair) MEFs. The indicated areas with white squares are enlarged approximately eightfold along each edge and are displayed on the right side of each pair of images. Scale bar = 5 μm (full), 625 nm (inset).

no relationship and are thus independently distributed. For example, we measured the LA fiber center to NPC center distance in WT cells compared with the expected distances assuming no relationship (Fig. 2 B; compare the measured data in the blue violin plot on top vs. the expected distances in the red violin plots on bottom). By examining the difference in the observed with the expected distributions (Fig. 2 C), we could see a paucity (green) or excess (purple) of NPCs at certain distances from the centers of LA fibers. For example, in a single WT nucleus, we observed fewer NPCs within 30 nm of the fibers and an excess of NPCs between 30 and 100 nm relative to the null hypothesis (Fig. 2 C WT, green area). To validate this approach, we performed the same analysis of the LA fiber to NPC distance in a single *Lmnb1*<sup>-/-</sup> MEF nucleus (Fig. 2 B). As in the WT nucleus, we saw an excess of NPCs between 30 and 100 nm in the *Lmnb1*<sup>-/-</sup> nucleus (Fig. 2 C). This agreed with the qualitative observation that the NPCs were associated with, but not colocalized with, lamin fibers (Fig. 1, A and B; and Fig. 2 A).

Measuring the distance from the lamin face centers to NPCs allowed us to more precisely determine how NPCs are related to the lamin fibers. The faces are delineated by the lamin fibers composing the lamin isoform meshwork (Fig. 2 A; Shimi et al., 2015). Their centers are points that are locally the most distant from the lamin fibers. This analysis also allowed us to account for changes in face size, such as the enlargement seen in *Lmnb1*<sup>-/-</sup> or *Lmna*<sup>-/-</sup> nuclei (Fig. 1 B and Fig. 2 A). Measuring both the distances of the NPCs to the lamin fibers and the centers of the faces allowed us to examine a 2D bivariate statistical distribution in a single nucleus (Fig. S1). To explore if the NPCs

also had a relationship with the center of the faces, we found the points the most distant from the lamin fibers within a local area (Fig. 2 A, white Xs). For a circle, this would be the center, but other shapes may have multiple centers (see Materials and methods). We measured the distances between the center of the NPCs and the center(s) of the faces (Fig. S1 G) and then compared that distribution with the null hypothesis (Fig. 2, D and E). In both the WT and the *Lmnb1*<sup>-/-</sup> nucleus, we observed median distances that were smaller than expected. This means that the NPCs were closer to the center of the faces than expected by chance. This is consistent with the observation that NPCs did not directly colocalize with the lamin fibers, but had a lateral proximal relationship.

We combined the distances of the NPCs to the lamin fibers and the distances of the NPCs from the face centers into 2D histograms to represent the bivariate distribution (Fig. S2). The 2D histograms showed that there was an expectation that NPCs would be near the LA fibers and away from the faces by chance in a broad distribution. However, the NPCs were offset from the LA fibers in a narrower-than-expected distribution (Fig. S1, A–F). In the WT MEFs, the negative correlation between the distances was also apparent, which is expected since the NPCs that are farther from the lamin fibers tend to be closer to the face centers (Fig. S1, A and B). However, the 2D histograms of single nuclei were sparse and noisy, indicating that additional distance measurements were needed for evaluation.

The localizations of both lamin fibers and NPCs were based on finding local maxima within the continuous reconstruction of the fluorescence intensity from critically sampled 3D-SIM images and were not dependent on rounding to the nearest pixel

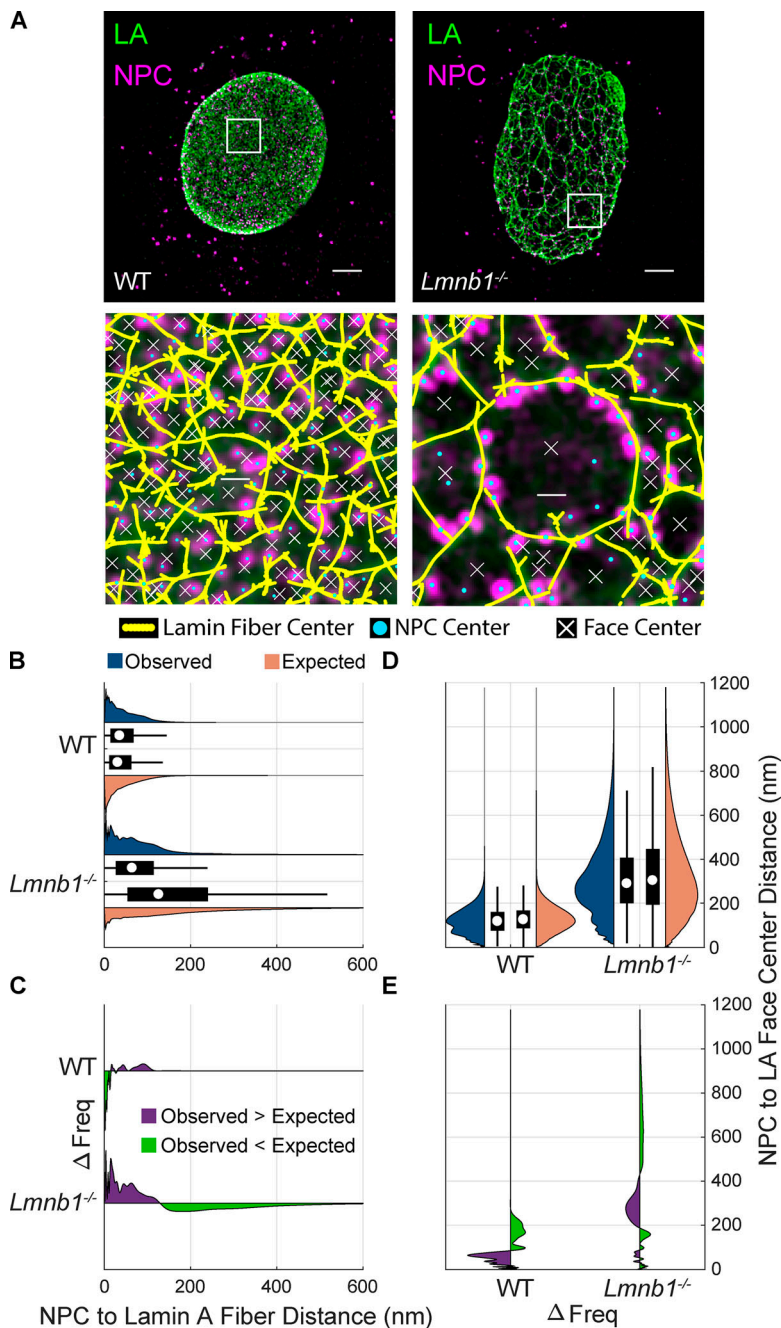


**Figure 2. Computational image analysis reveals that NPCs are closely associated with LA fibers. (A–E)** Each plot reflects a single nucleus and is meant to illustrate the analysis process rather than show a representative distribution as in later figures. **(A)** Immunofluorescence images labeling LA (green) and NPCs (magenta) of WT and *Lmnb1*<sup>-/-</sup> MEF nuclei as in Fig. 1 were subjected to computational image analysis. White boxes in the top row are magnified eight times along each edge. The centers of LA fibers (yellow lines), NPCs (cyan dots), and faces (white Xs) were segmented to subpixel precision (Kittisopikul et al., 2020); Materials and methods). Scale bar = 5  $\mu$ m (full), 625 nm (inset). **(B)** Paired violin and box plots of NPC to LA fiber distances for the nuclei in A. The violin (blue) and box plots on top represent the observed distance distributions. The violin (red) and box plots on bottom represent the expected distance distributions under the null hypothesis. The white circle indicates the median. The thick black bar indicates the interquartile range (IQR). The black whiskers indicate 1.5 times the IQR. **(C)** Frequency (Freq) difference plot of observed minus expected LA fiber to NPC distances. The green portion below the line indicates where the observed frequency is less than expected. The purple portion above the line indicates where the observed frequency is greater than expected. **(D)** NPC to LA face center distances displayed as in B, rotated 90° counterclockwise. **(E)** Frequency difference plot of NPC to LA face center distances, displayed as in C, rotated 90° counterclockwise.

(see Materials and methods and online supplemental materials; Kittisopikul et al., 2020). Here, we focused on localizing lamin fibers and NPCs resolved by 3D-SIM and not their specific molecular components consisting of individual 3.5-nm lamin filaments (Turgay et al., 2017) and/or specific nucleoporins. Furthermore, we measured the distance between structures localized within two channels separated by their chromatic properties; thus, these distance measurements were not limited by resolution (Stelzer, 1998). The main limitations to the precision of the localization and distance measurements are the inaccuracy of indirect immunofluorescence labeling, signal-to-noise ratio, and structured illumination microscopy reconstruction artifacts. This was mitigated by examining the distribution of tens of thousands of distance measurements. These analyses permitted us

to express the magnitude of differences in the codistributions, or the lack thereof, in terms of nanometers with high statistical power (see Materials and methods).

#### LA and LB1 fibers have a more pronounced relationship with NPCs than LC and LB2 fibers do in WT MEFs

We previously found that the four main lamin isoforms (LA, LC, LB1, and LB2) form independent meshworks (Shimi et al., 2015), and we sought to see if each isoform had a distinct relationship with NPCs. Having established our approach to analyzing lamin–NPC associations, we measured the distances between the center of individual NPCs and the center of the nearest lamin fiber across the surface of the nucleus closest to the coverslip of 10 WT nuclei for each lamin isoform. Overall, the data obtained

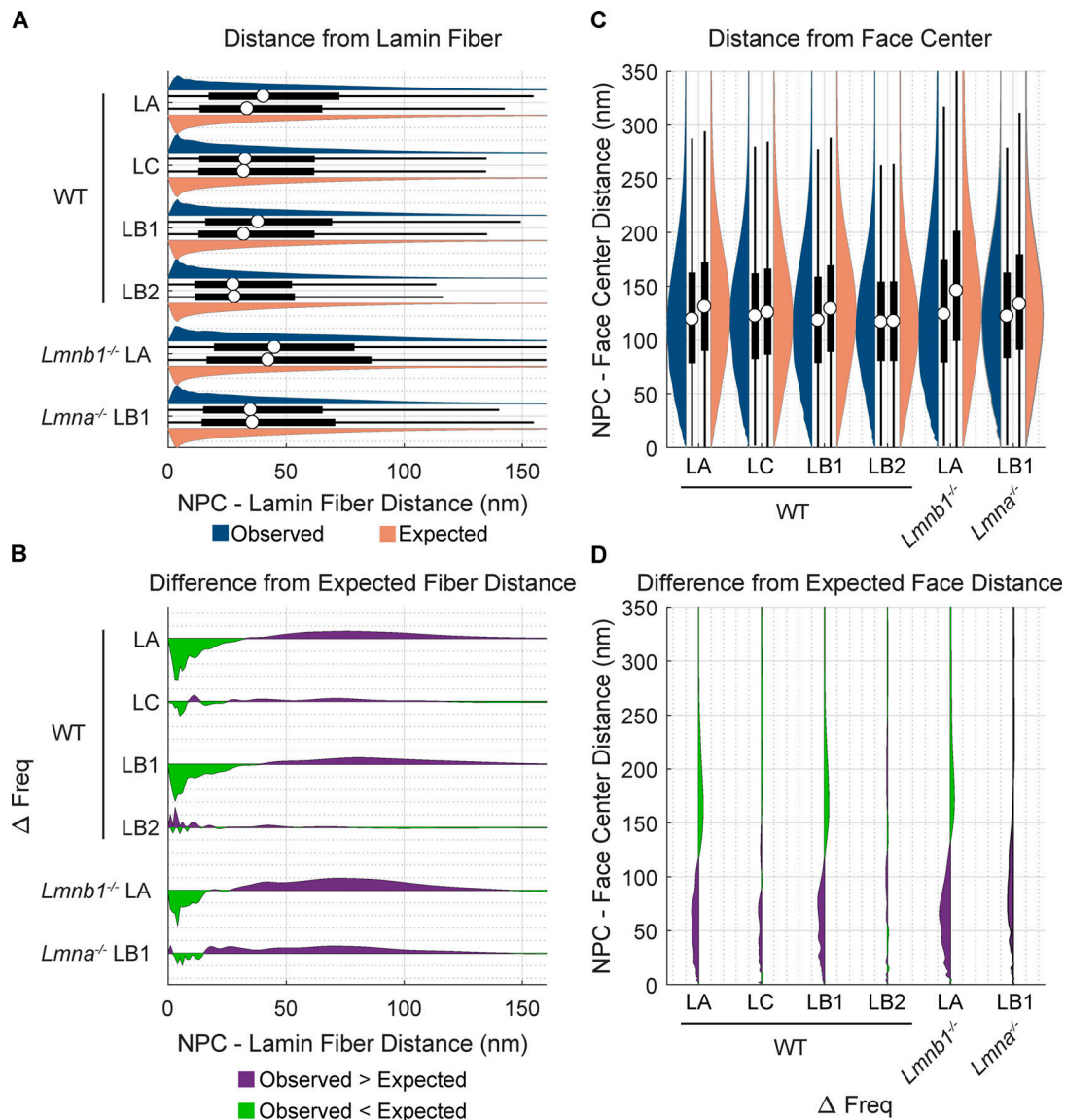


**Figure 3. Quantitative analysis of lamin–NPC distances over many nuclei reveals NPCs are offset from the center of LA and LB1 fibers in WT, *Lmna*<sup>-/-</sup>, and *Lmnb1*<sup>-/-</sup> MEFs by 20–30 nm. (A) Paired violin and box plots of NPC to lamin fiber distances. The violin (blue) and box plots on top represent the observed distance distributions. The violin (red) and box plots on bottom represent the expected distance distributions under the null hypothesis. The white circles indicate the medians. The thick black bar indicates the interquartile range (IQR). The black whiskers indicate 1.5 times the IQR. (B) Frequency (Freq) difference plots of observed minus expected lamin fiber to NPC distances. The green portion below the line indicates where the observed frequency is less than expected. The purple portion above the line indicates where the observed frequency is greater than expected. (C) NPC to lamin face center distances displayed as in A, rotated 90° counterclockwise. (D) Frequency difference plot of NPC to lamin face center distances, displayed as in C, rotated 90° counterclockwise. Each violin or box plot represents 10 cells with the number of NPCs detailed in Table 1.**

support the lack of direct colocalization between NPCs and lamin fibers, which we observed qualitatively and quantitatively in single nuclei (Fig. 1 and Fig. 2). The median distances from the centers of NPCs to the centers of LA fibers (40.4 nm;  $P < 0.001$ ; Fig. 3 A, Fig. S2 A, and Table 1) and to the centers of LB1 fibers (38.1 nm;  $P < 0.001$ ; Fig. 3 A and Table 1) were similar. The observed median distances were 6 nm greater than the expected distribution (+6.9 nm LA; +6.0 nm LB1; Fig. 3, A and B; Fig. S2 C; and Table 1). The expected distribution represents the distances between NPCs and lamins that we would expect under the null hypothesis that there is no relationship between the position of

NPCs and lamins. It was calculated by a Monte Carlo simulation randomly placing an NPC within the segmented area of the nucleus. The median distance between NPCs and the center of faces in the LA meshworks was similar (119.3 nm; -11.7 nm vs. expected;  $P < 0.001$ ; Table 2) to LB1 (118.3 nm; -10.8 nm vs. expected;  $P < 0.001$ ; Table 2), and both median distances were less than expected if the lamins and NPCs were not associated (Fig. 3 C and Table 2). These data show that NPCs and LA or LB1 fibers are not directly colocalized but have a proximal lateral relationship. These findings suggest that NPCs and LA or LB1 fibers are structurally linked within the NL.

Table 1. Lamin fiber–NPC center to center distance distributions for WT, *Lmnb1*<sup>-/-</sup>, and *Lmna*<sup>-/-</sup> MEFs

Cell	Lamin	Observed (nm)		Expected (nm)		Observed – expected (nm)		P values		No. of NPCs
		Median	SD	Median	SD	Median	SD	Median	SD	
WT	LA	40.4	38.0	33.5	56.5	6.9	-18.5	0.00		14,780
WT	LC	32.8	35.0	32.1	49.4	0.7	-14.5	0.37 <sup>a</sup>	0.01 <sup>a</sup>	11,459
WT	LB1	38.1	36.2	32.1	56.9	6.0	-20.7	0.00		15,150
WT	LB2	27.6	29.2	28.1	38.7	-0.6	-9.6	0.00		17,146
<i>Lmnb1</i> <sup>-/-</sup>	LA	45.1	48.6	42.4	216.8	2.7	-168.2	0.59 <sup>a</sup>	0.00	11,971
<i>Lmna</i> <sup>-/-</sup>	LB1	34.9	34.5	35.8	297.7	-0.8	-263.1	0.00		9,740

Median and SD of the observed and expected lamin fiber to NPC center to center distances, the difference between them, P values (see Materials and methods), and number of NPCs. The data in each row were collected from 10 cells. The Mann-Whitney *U* test and Ansari-Bradley test were used as described in Materials and methods.

<sup>a</sup>P values above the Bonferroni corrected  $\alpha$  value of 0.05/8 tests = 0.006.

In contrast to the relationships between the NPCs and LA or LB1, the median distance from LC fibers to NPC centers did not differ significantly from expected (32.8 nm observed, +0.7 nm vs. expected;  $P = 0.37$ ; Fig. 3 A, Fig. S2 B, and Table 1). Also, the SD of distances between LC fibers and NPCs (35.0 nm observed, -14.5 nm vs. expected;  $P = 0.01$ ; Fig. 3 A and Table 1) was not significant when using a Bonferroni-corrected  $\alpha$  level. While the P value of 0.01 is smaller than the traditional  $\alpha$  level of 0.05, we conducted multiple comparisons and thus need to compensate for Type I error. The Bonferroni correction of the  $\alpha$  level across the 12 pairs of distributions compared in Table 1 and Table 2 leads to an  $\alpha$  level of  $0.05/12 \approx 0.004$ . However, the median distance determined for the NPC center to LC face center differed from the expected distribution (122.4 nm observed, -3.3 nm vs. expected;  $P < 0.001$ ; Fig. 3 C and Table 2). While these measurements followed a pattern similar to that detected for LA and LB1, the magnitude of the differences was much smaller for LC (Fig. 3, C and D; and Table 2). Overall, these data suggest that the offset between NPCs and LC fibers is closer (median: 32.8 nm) than that between NPCs and LA or LB1 fibers (medians: 40 nm). However, given the small differences in the LC fiber to NPC

center measurements relative to expected, we cannot completely reject the null hypothesis for the LC fiber to NPC distances.

The relationship between LB2 fibers and NPCs in WT MEFs differed from the relationships between the other lamin isoforms and NPCs. We observed a statistically significant difference in medians from expected distributions between the centers of LB2 fibers and NPCs (27.6 nm observed; -0.6 nm vs. expected;  $P < 0.001$ ; Fig. 3 A, Fig. S2 D, and Table 1). However, the shift was an order of magnitude less and in the opposite direction than observed for LA and LB1 fibers. The median distance from NPCs to LB2 face centers (116.7 nm observed; -0.6 nm vs. expected; Fig. 3 C and Table 1) was not significantly different from what was expected. These findings suggest that there is no obvious relationship between the distribution of LB2 fibers and NPCs, or if there is, it cannot be discerned in our analyses.

#### Knocking out *Lmna* affects the LB1–NPC relationship more than knocking out *Lmnb1* affects the LA–NPC relationship

The results presented in the previous section show a clear spatial relationship between both LA and LB1 fibers and NPCs in the dense meshworks of WT MEF nuclei. Either the removal of LA

Table 2. Face–NPC center to center distance distributions for WT, *Lmnb1*<sup>-/-</sup>, and *Lmna*<sup>-/-</sup> MEFs

Cell	Lamin	Observed (nm)		Expected (nm)		Observed – expected (nm)		P values		No. of NPCs
		Median	SD	Median	SD	Median	SD	Median	SD	
WT	LA	119.3	62.6	130.9	78.3	-11.7	-15.7	0.00		14,780
WT	LC	122.4	57.1	125.7	69.0	-3.3	-11.9	0.00		11,459
WT	LB1	118.3	56.8	129.1	76.0	-10.8	-19.2	0.00		15,150
WT	LB2	116.7	51.5	117.3	58.9	-0.6	-7.3	0.25 <sup>a</sup>	0.08 <sup>a</sup>	17,146
<i>Lmnb1</i> <sup>-/-</sup>	LA	124.0	90.0	146.0	235.2	-22.0	-145.2	0.00		11,971
<i>Lmna</i> <sup>-/-</sup>	LB1	122.1	55.7	133.2	304.3	-11.1	-248.6	0.00		9,740

Median and SD of the observed and expected lamin face to NPC distances, the difference between them, P values (see Materials and methods), and number of NPCs. The data in each row were collected from 10 cells. The Mann-Whitney *U* test and Ansari-Bradley test were used as described in Materials and methods.

<sup>a</sup>P values above the Bonferroni corrected  $\alpha$  value of 0.05/7 tests = 0.007.

and LC by knocking out *Lmna* or the removal of LB1 by knocking out *Lmnb1* in MEFs leads to dramatic changes in the remaining lamin meshwork characteristics, most notably an increase in the lamin mesh size (Fig. 2; Shimi et al., 2015). Because the lamin fibers have close structural relationships with NPCs, we next wanted to determine if these relationships are altered when the lamin meshwork structure changes.

We analyzed the spatial relationships between LA fibers and NPCs in 10 *Lmnb1*<sup>-/-</sup> nuclei using the same quantitative methods applied to our studies of WT nuclei. In *Lmnb1*<sup>-/-</sup> nuclei, there was a greater median distance between LA fiber centers and NPC centers than expected (45.1 nm observed; +2.7 nm vs. expected; Fig. 3 A, Fig. S3 A, and Table 1); however, this shift in medians was not statistically significant ( $P = 0.59$ ; Table 1). Interestingly, a statistical test comparing the SDs showed that the distributions are significantly different (48.6 nm observed; -168.2 nm vs. expected;  $P < 0.001$ ; Fig. 3, A and B; and Table 1). This reflects the long tail of the expected distributions, since under the null hypothesis some NPCs may appear in the middle of the faces of the enlarged LA meshworks, that is, farther away from the lamin fibers. The median distance of NPCs from the LA face centers was less than expected by a large magnitude (124.0 nm; -22.0 nm vs. expected;  $P < 0.001$ ; Fig. 3, C and D; and Table 2). This difference is due to the distribution of the offsets of the NPCs from the lamin fibers, which is larger than the expected offset distributions where more NPCs were closer to the lamin fibers. The observed distance distributions of WT and *Lmnb1*<sup>-/-</sup> MEFs (Fig. 3 A) both differ from the expected distributions under the null hypothesis in a similar manner (Fig. 3 B). This indicates that in *Lmnb1*<sup>-/-</sup> nuclei, the proximal lateral relationship between LA fibers and NPCs remains, although the median distance between LA fibers and NPCs increased by 5 nm. Overall, this suggests that the distance between the centers of LA fibers and NPCs does not depend strongly on the presence of LB1 fibers.

The measured distances in *Lmnb1*<sup>-/-</sup> MEFs showed a relationship between LA and NPCs similar to the relationship between LA and NPCs in WT MEFs. Distances <30 nm between LA fibers and NPCs occurred less frequently than expected (Fig. 3 B, green area), and distances 50–100 nm (Fig. 3 B, purple area) occurred more frequently than expected. This differed from the analysis of the single nucleus, which consisted mostly of enlarged faces (Fig. 3), whereas most nuclei typically had a mix of small and large faces (Fig. 2).

In *Lmna*<sup>-/-</sup> MEFs, we observed a pattern of distances between NPCs and LB1 fibers reflecting a relationship similar to that observed in WT MEFs. The median distances between the centers of LB1 fibers and NPCs in *Lmna*<sup>-/-</sup> MEFs matched the expected distribution (34.9 nm observed; -0.8 vs. expected;  $P < 0.001$ ; Fig. 3, A and B; Fig. S3 B; and Table 1), initially calling into question whether a relationship existed between NPCs and LB1 fibers in *Lmna*<sup>-/-</sup> MEFs. However, the SD of LB1 fiber to NPC medians in *Lmna*<sup>-/-</sup> MEFs did differ significantly from expected (34.9 nm observed; -263.1 nm vs. expected;  $P < 0.01$ ; Fig. 3, A and B; and Table 1), reflecting the enlarged faces in *Lmna*<sup>-/-</sup> MEFs. Recall that in contrast, the LB1 fiber to NPC median distances in WT MEFs were slightly larger and differed from the expected (38.1 nm;  $P < 0.001$ ; Fig. 3 A and Table 1). Additionally, the difference between the frequencies of the observed and expected

distributions was smaller in magnitude in *Lmna*<sup>-/-</sup> MEFs compared with WT MEFs, along with a small positive peak suggesting some colocalization (Fig. 3 B). LB1 face center to NPC center distances were significantly different from expected, with a large change in magnitude (122.1 nm observed; -11.1 nm vs. expected;  $P < 0.001$ ; Fig. 3, C and D; and Table 2). As in WT MEFs, this reflects a lateral proximal relationship between LB1 fibers and NPCs in *Lmna*<sup>-/-</sup> MEFs. To summarize, the measured distances suggest the NPCs are positioned next to LB1 fibers and not within the fibers in both WT and *Lmna*<sup>-/-</sup> MEFs.

The average number of NPCs per nucleus in a single focal plane closest to the coverslip was reduced to 1,000 NPCs in *Lmna*<sup>-/-</sup> MEFs compared with 1,200 in *Lmnb1*<sup>-/-</sup> MEFs and 1,500 in WT MEFs (Fig. S4 A and Table 1), suggesting that *Lmna* and *Lmnb1* or their protein products (LA, LC, and LB1) are involved in regulating NPC number. Knocking out *Lmna* had a less-pronounced effect on NPC density, suggesting that change in NPC number may be related to changes in the size of the nucleus or cell cycle effects (Fig. S4 B). *Lmnb2*<sup>-/-</sup> MEFs had comparable NPC numbers and density to WT MEFs, implying that *Lmnb2* has a minimal effect on NPC number and density.

#### cryo-ET and immunogold labeling show LA/LC and LB1 filaments contacting the nucleoplasmic ring of NPCs

To further investigate the relationship between lamin filaments and NPCs, we performed cryo-ET of WT MEFs coupled with immunogold labeling of both LA/LC and LB1. The higher resolution of cryo-ET over light microscopy allowed us to assess the relative abundance of LA/LC and LB1 filaments contacting the NPC at the molecular level. We use the term lamin “filaments” to describe the molecular structures of lamins observed using cryo-ET. In contrast, lamin “fibers” refers to a grouping of these filaments that is resolvable using light microscopy. For the tomographic analysis, we extracted 340 nm × 340 nm × 20 nm subtomograms around the nucleoplasmic ring of NPCs (Fig. 4 A; Turgay et al., 2017) and counted the number of LA/LC or LB1 filaments using immunogold labeling (Fig. 4 B; Turgay et al., 2017). We observed more LA/LC filaments than LB1 filaments in these regions (Fig. 4 C). In the 24 volumes around NPCs, we observed 188 LA/LC labels and only 28 LB1 labels. This results in a ratio of 6.7 LA/LC labels for every LB1 label in volumes near NPCs. For comparison, in nine randomly selected volumes with immunogold labeling without NPCs (Turgay et al., 2017), we observed 140 LA/LC labels and 83 LB1 labels. This results in a ratio of 1.69 LA/LC labels for every LB1 label in volumes not near NPCs. This suggests an enrichment of approximately fourfold in the ratio of LA/LC to LB1 filaments near NPCs versus volumes lacking NPCs. This enrichment suggests a bona fide preference for LA/LC fibers over LB1 fibers contacting NPCs rather than one merely due to differences in the affinities of the antibodies used. These results also demonstrate that both LA and LB1 fibers are closely associated with the nucleoplasmic ring.

#### Organizational changes in LA meshworks and NPCs differ in response to silencing the expression of ELYS, TPR, and NUP153

The cryo-ET observations taken together with the demonstration that there was a proximal lateral association between NPCs

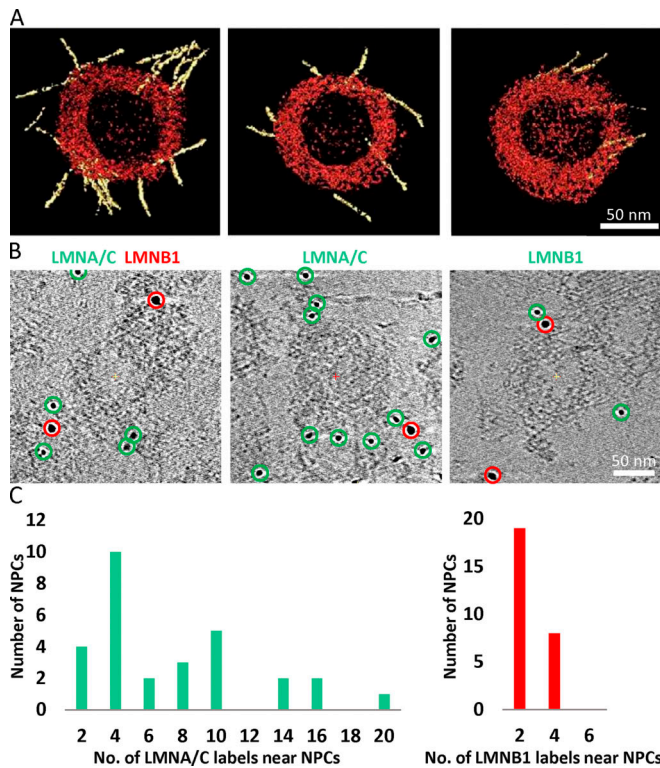


**Figure 4. Cryo-ET showing LA/LC and LB1 filament contacts with the nucleoplasmic ring. (A)** Lamin filaments (yellow) interact with NPCs (red) as seen by surface rendering representations of cryo-subtomograms. **(B)** Gold labeling of lamin filaments observed by cryo-ET. The position of LA/LC labels (green) and LB1 labels (red) are indicated. Double labeling (left) or labeling of individual lamin isoforms was analyzed and presented as histograms. The unmarked gold particles (middle, right) are fiducial markers. **(C)** A total number of 214 LA/LC labels and 70 LB1 labels were detected around 47 nucleoplasmic rings.

and both LA and LB1 fibers suggest that there are attachments of lamin filaments to nucleoplasmic components of NPCs. We next explored the potential roles of individual nucleoporins in attaching lamin fibers to the NPCs. For these studies, we focused on ELYS, NUP153, and TPR, all components of the nucleoplasmic NPC structures that are in close proximity to the lamina (Roux et al., 2012). The nucleoporin ELYS is a component of the nucleoplasmic ring of NPCs and is required for postmitotic NPC assembly, where it binds to the chromosomes and recruits the Nup107-160 complex of the nucleoplasmic ring (Franz et al., 2007). TPR and NUP153 are both components of the nuclear basket structure of the NPC that associates with the nucleoplasmic ring (Duheron et al., 2014; Krull et al., 2004). We employed siRNA knockdown (KD) of each nucleoporin consisting of two rounds of 48 h each (96 h in total), as detailed in the Materials and methods, to determine their potential roles in linking the NPC to lamin fibers (Fig. S6). We believe all cells had gone through at least one cycle of mitosis during this 96-h period. We evaluated the efficacy of the KD by Western blot of whole cell lysates, resulting in reductions of the amount of each protein by 75%, 50%, or 40% for NUP153, ELYS, or TPR, respectively (Fig. S5). KD of either ELYS or TPR led to significant changes in NPC distribution and structural relationship to the LA fibers. The

most dramatic effect was the reorganization of NPCs into clusters after ELYS KD (Fig. 5 A). Individual fluorescent puncta could still be resolved within each cluster, indicating that some NPC structure was likely retained. In contrast, siRNA KD of NUP153 or TPR did not cause NPC clustering in WT MEFs (Fig. 5 A). The median distance between the centers of NPCs and LA fibers in ELYS-depleted cells (70.8 nm; +20 nm vs. scrambled;  $P < 0.001$ ; Fig. 5, A and B; Fig. S6; and Table 3) increased compared with scrambled siRNA controls (50.9 nm;  $P < 0.001$ ; Fig. 5, A and B; Fig. S6; and Table 3). Additionally, the median distance between face centers of the LA fiber meshwork and the NPCs was reduced (89.7 nm; Fig. 5 C and Table 4) compared with scrambled siRNA (106.2 nm;  $P < 0.001$ ; Fig. 5 C, Fig. S6, and Table 4). These data suggest that LA fibers were being excluded from the ELYS-depleted NPC clusters such that these clusters became located in large faces within the LA meshwork. Interestingly, the size of faces contained within the LA meshwork also appeared to increase upon ELYS KD (Fig. 5, A and F). As a measure of lamin face size, we summed the NPC to fiber distances and the NPC to face center distances, since, for a perfectly circular face in the meshwork, this quantity would be the radius of the circle with respect to each NPC. The face radius of the LA fiber meshwork (169.7 nm; Table 5) significantly increased versus the scrambled siRNA control (163.3 nm;  $P < 0.001$ ; Table 5) upon ELYS KD, indicating that the LA meshwork expanded when ELYS was depleted.

While there did not appear to be NPC clustering upon TPR depletion, the NPCs appeared to be less associated with the LA fibers and more centered within the faces of a dense LA meshwork (Fig. 5 A). The median distance between the centers of NPCs and LA fibers with TPR KD (59.0 nm; Fig. 5, B and C; Fig. S6; and Table 3) increased versus a scrambled siRNA control, though to a lesser magnitude than for ELYS KD (+8.2 nm TPR KD vs. +20.0 nm ELYS KD;  $P < 0.001$ ; Fig. 5, B and C; and Table 3). The median distance between NPCs and LA face centers (90.0 nm; Fig. 5 D and Table 4) was reduced with TPR KD (-16.2 nm;  $P < 0.001$ ; Fig. 5, D and E; and Table 4). The face radius of the LA fiber meshwork (154.3 nm;  $P < 0.001$ ; Table 5) was decreased upon TPR depletion (-9.1 nm;  $P < 0.001$ ; Table 5). These data suggest that the NPCs were less closely associated with LA fibers following TPR KD and tended to be in the middle of small faces of the LA meshwork. This suggests a structural role for TPR where it may contribute to a defined spacing between LA fibers and NPCs.

In contrast to ELYS and TPR KDs, NUP153 KD only slightly reduced the median distance between NPCs and LA fibers (-0.8 nm;  $P < 0.001$ ; Fig. 5, B and C; and Table 3). This reduction was an order of magnitude smaller than observed for the KD of either ELYS or TPR. The distance between LA face centers and NPCs was reduced (-6.5 nm;  $P < 0.001$ ; Fig. 5, D and E; Fig. S6; and Table 4), and the face radius for the LA meshwork was reduced (-7.5 nm;  $P < 0.001$ ; Table 5). The faces in the LA meshwork appeared smaller and more compact than the faces in controls, which was similar to the effect seen with TPR KD. Thus, upon NUP153 KD, the faces in the LA meshwork became smaller than those in the scramble control, modestly decreasing both the LA fiber-NPC and LA face-NPC distances.

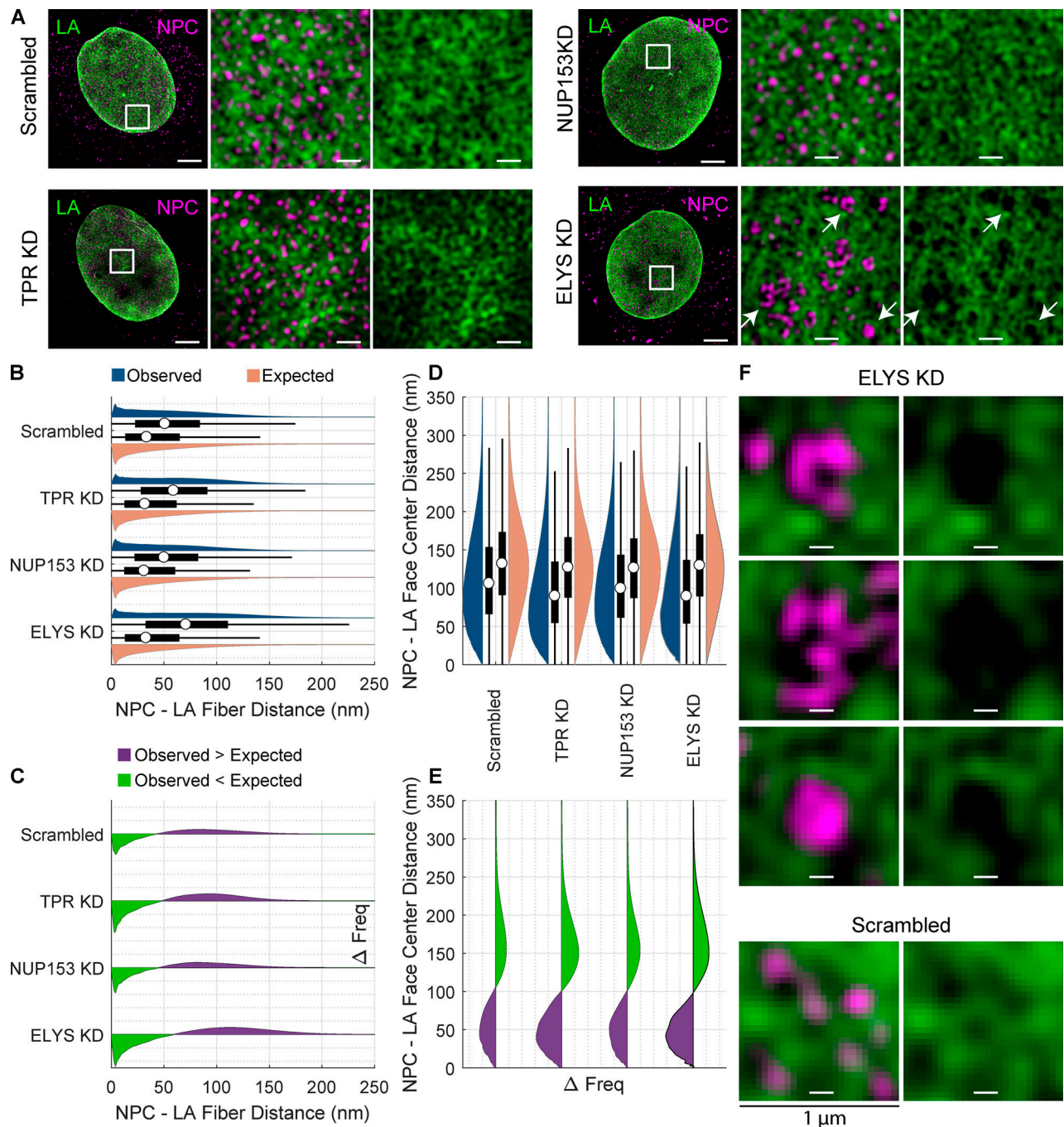


**Figure 5. Co-distribution of LA and NPC components after siRNA transfection shows enlarged LA meshworks filled with NPC clusters upon ELYS KD.**

**(A)** Immunofluorescence images of LA (green) and NPCs (magenta) following KDs of TPR, NUP153, ELYS, and scramble control. Note the clustering of NPCs in the ELYS KD. Area of white box (left) is shown merged (center) and just lamin (right). White arrows indicate areas of NPC clustering. Scale bar = 5  $\mu$ m (full), 625 nm (inset). **(B)** Paired violin and box plots of NPC center to LA fiber center distances. The violin (blue) and box plots represent the observed distance distributions. The violin (red) and box plots on bottom represent the expected distance distributions under the null hypothesis. The white circle indicates the median. The thick black bar indicates the interquartile range (IQR). The black whiskers indicate 1.5 times the IQR. **(C)** Frequency (Freq) difference plots of observed minus expected LA fiber to NPC distances for the KD series. The green portion below the line indicates where the observed frequency is less than expected. The purple portion above the line indicates where the observed frequency is greater than expected. **(D)** NPC center to LA face center distances displayed as in B, rotated 90° counterclockwise. **(E)** Frequency difference plot of NPC to LA face center distances, displayed as in C, rotated 90° counterclockwise. **(F)** 1- $\mu$ m<sup>2</sup> areas around NPC clusters formed after scramble treatment or ELYS KD indicated by white arrows in A shown merged (left) and just lamin (right). Each violin or box plot represents 20 cells with the number of NPCs detailed in Table 3. Scale bar = 150 nm.

Table 3. Lamin fiber to NPC center to center distance distributions of WT MEFs with TPR, NUP153, and ELYS KD

siRNA KD	Lamin Labeled	Observed (nm)		Expected (nm)		Observed – expected (nm)		P value vs. expected Median	Observed – scrambled Median (nm)	P value vs. scrambled Median	No. of NPCs N
		Median	SD	Median	SD	Median	SD				
Scrambled	LA	50.9	39.5	33.6	40.4	17.3	-0.9	0.00			39,096
TPR KD	LA	59.0	39.5	31.9	36.9	27.1	2.6	0.00	8.2	0.00	40,767
NUP153 KD	LA	50.1	38.6	31.1	35.7	19.0	2.8	0.00	-0.8	0.00	36,066
ELYS KD	LA	70.8	48.9	32.9	42.4	37.9	6.5	0.00	20.0	0.00	21,521
Scrambled	LC	42.9	36.1	31.7	42.6	11.2	-6.5	0.00			37,760
TPR KD	LC	56.6	38.1	31.2	54.4	25.4	-16.2	0.00	13.7	0.00	35,489
NUP153 KD	LC	39.9	35.1	29.8	35.6	10.1	-0.5	0.00	-3.0	0.00	39,988
ELYS KD	LC	63.1	46.7	32.8	44.2	30.3	2.6	0.00	20.2	0.00	27,053
Scrambled	LB1	51.6	42.4	35.4	51.8	16.2	-9.4	0.00			37,383
TPR KD	LB1	52.1	38.4	31.3	49.0	20.8	-10.6	0.00	0.5	0.00	40,899
NUP153 KD	LB1	46.9	41.3	35.2	40.6	11.7	0.7	0.00	-4.7	0.00	31,145
ELYS KD	LB1	48.5	40.1	31.1	40.6	17.4	-0.5	0.00	-3.1	0.00	24,981
Scrambled	LB2	30.1	33.8	34.4	67.2	-4.4	-33.4	0.00			35,444
TPR KD	LB2	28.6	30.3	30.2	75.0	-1.7	-44.7	0.00	-1.5	0.00	36,974
NUP153 KD	LB2	25.6	30.9	32.3	39.9	-6.6	-9.0	0.00	-4.4	0.00	31,628
ELYS KD	LB2	34.2	33.8	31.2	40.2	3.0	-6.3	0.00	4.1	0.00	25,215

Median and SD of the observed and expected lamin fiber to NPC center to center distances, the difference between them, P values (see Materials and methods), and number of NPCs. The distributions were also compared with scrambled siRNA controls. The data in each row were collected from 20 cells. The Mann-Whitney *U* test and Ansari-Bradley test were used as described in Materials and methods.

The effect of NUP153 KD is similar to that of TPR KD but reduced in magnitude.

#### Changes in LC meshworks are similar to those in LA meshworks but of lesser magnitude following silencing of ELYS, TPR, and NUP153

Our analysis of LC fibers and NPCs suggested that LC fibers do not have a definable relationship with NPCs in WT MEFs (see Fig. 3). However, the codistribution of LC fibers and NPCs was significantly modified by KD of either ELYS or TPR. ELYS KD resulted in an increase in the median distance between NPCs and LC fibers (63.1 nm; +20.2 nm vs. scrambled;  $P < 0.001$ ; Fig. 6, A–C; Fig. S7; and Table 3), and the LC face center to NPC center distances decreased (96.1 nm; -13.0 nm vs. scrambled;  $P < 0.001$ ; Fig. 6, D–F; and Table 4). The KD of ELYS also increased the effective face radius (167.5 nm; +10.5 nm vs. scrambled;  $P < 0.001$ ; Table 5), indicating that ELYS KD results in expanded LC meshworks as it did for LA meshworks. These results suggest that the NPC clusters induced by ELYS depletion exclude LC fibers as well as LA fibers.

siRNA KD of TPR resulted in an increase in the median distance between NPCs and LC fibers (+13.7 nm vs. scramble;  $P < 0.001$ ; Fig. 6, B and C; Fig. S7; and Table 3), a decrease in median distances between NPCs and LC face centers (-19.2 nm;  $P < 0.001$ ; Fig. 6, D and E; and Table 4), and a decrease in the effective face radius (-6.2 nm;  $P < 0.001$ ; Table 5). These results indicate that the LC meshwork face size decreased after TPR KD, similar to LA.

NUP153 KD resulted in a decrease (-3.0 nm;  $P < 0.001$ ; Fig. 6, B and C; Fig. S7; and Table 3) in the median distance between NPCs and LC fibers. Decreases in LC face to NPC center distances (-2.2 nm;  $P < 0.001$ ; Fig. 6, D and E; and Table 4) and face radius were also detected (-4.1 nm;  $P < 0.001$ ; Table 5). While these decreases are consistent with the change seen in the distances between NPCs and LA fibers, the magnitude of the change is much less than that for depletion of ELYS or TPR. Overall, the observed changes in the NPC distribution relative to LC fibers upon ELYS, TPR, and NUP153 KD were similar to those observed for LA fibers.

Depletion of TPR or NUP153 results in denser LB1 meshworks, while LB1 fibers protrude into NPC clusters upon ELYS KD. Depletion of TPR, NUP153, or ELYS altered the median center to center distance between LB1 fibers and NPCs (+0.5 nm, -4.7 nm, and -3.1 nm, respectively, Observed-Scrambled;  $P < 0.001$ ; Fig. 7, A and B; Fig. S8; and Table 3) relative to scrambled siRNA controls. The small magnitude of these changes suggests that depletion of these nucleoporins had a minimal impact on the relationship between LB1 and NPCs compared with the changes seen in the distances between NPCs and LA/LC fibers (Fig. 7 C). In contrast, the changes in median distance between LB1 face centers and NPCs were larger in magnitude upon KD of TPR, NUP153, or ELYS (-19.2 nm, -2.5 nm, and -13.0 nm, respectively; Observed-Scrambled;  $P < 0.001$ ; Fig. 7, D–F; Fig. S8; and Table 4), and face radii decreased (-20.3 nm, -1.1 nm, -17.6 nm, respectively; Observed-Scrambled;  $P < 0.001$ ; Table 5).

Table 4. Lamin face to NPC center to center distance distributions of WT MEFs with TPR, NUP153, and ELYS KD

siRNA	Lamin	Observed (nm)		Expected (nm)		Observed – expected (nm)		P value vs. expected	Observed – scrambled	P value vs. scrambled	No. of NPCs
		Median	SD	Median	SD	Median	SD				
KD	Labeled							Median	Median (nm)	Median	N
Scrambled	LA	106.2	60.6	132.0	63.6	-25.8	-3.0	0.00			39,096
TPR KD	LA	90.0	58.0	127.1	60.0	-37.1	-2.0	0.00	-16.2	0.00	40,767
NUP153 KD	LA	99.7	57.0	126.2	58.0	-26.6	-1.1	0.00	-6.5	0.00	36,066
ELYS KD	LA	89.7	58.8	129.7	64.4	-39.9	-5.6	0.00	-16.4	0.00	21,521
Scrambled	LC	109.1	58.1	126.5	65.2	-17.4	-7.2	0.00			37,760
TPR KD	LC	89.9	55.6	125.8	73.4	-35.9	-17.7	0.00	-19.2	0.00	35,489
NUP153 KD	LC	106.6	55.5	122.9	57.7	-16.3	-2.2	0.00	-2.5	0.00	39,988
ELYS KD	LC	96.1	59.3	129.9	65.9	-33.7	-6.6	0.00	-13.0	0.00	27,053
Scrambled	LB1	114.0	63.4	138.6	73.4	-24.6	-9.9	0.00			37,383
TPR KD	LB1	96.7	56.9	126.6	68.4	-30.0	-11.4	0.00	-17.3	0.00	40,899
NUP153 KD	LB1	118.8	63.7	135.8	65.7	-17.0	-2.0	0.00	4.8	0.00	31,145
ELYS KD	LB1	101.5	58.2	125.6	62.2	-24.1	-4.0	0.00	-12.5	0.00	24,981
Scrambled	LB2	138.8	59.7	134.6	85.8	4.2	-26.1	0.00			35,444
TPR KD	LB2	125.2	54.8	124.1	90.0	1.1	-35.1	0.00	-13.6	0.00	36,974
NUP153 KD	LB2	139.7	60.4	129.1	64.1	10.6	-3.7	0.00	0.9	0.00	31,628
ELYS KD	LB2	120.6	56.4	126.5	62.4	-5.9	-6.0	0.00	-18.2	0.00	25,215

Median and SD of the observed and expected lamin face to NPC distances, the difference between them, P values (see Materials and methods), and number of NPCs. The distributions were also compared with scrambled siRNA controls. The data in each row were collected from 20 cells. The Mann-Whitney *U* test and Ansari-Bradley test were used as described in Materials and methods.

Knocking down TPR or ELYS decreased the distances between NPCs and LB1 face centers as well as the LB1 face radii, while knocking down NUP153 had less impact.

Visual inspection of the accompanying images reveals denser LB1 meshworks upon TPR and NUP153 depletion relative to scrambled siRNA controls, as the numerical analysis suggests, but also enlarged faces upon ELYS KD in contrast with the quantitative measurements. Closer inspection of the images upon ELYS depletion reveals LB1 fibers protruding into the enlarged faces (Fig. 7). This is not seen in the enlarged faces of LA/LC meshworks (Fig. 5 A and Fig. 6 A). The interdigitation of LB1 fibers within the NPC clusters explains why an increase in LB1 fiber to NPC distances is not seen quantitatively.

#### Depletion of ELYS, TPR, or NUP153 has a minor impact on the independence between LB2 fibers and NPCs

As described in previous sections, we could not detect a relationship between LB2 fibers and NPCs in WT MEFs (see Fig. 3). Upon KD of TPR, NUP153, or ELYS, the observed distances between LB2 fibers and NPCs differed by a few nanometers from expected (-1.7 nm, -6.6 nm, and +3.0 nm, respectively; Observed-Expected;  $P < 0.01$ ; Fig. 8, A and B; Fig. S9; and Table 3,) and from the scramble control (-1.5 nm, -4.4 nm, and +4.1 nm, respectively; Observed-Scrambled;  $P < 0.01$ ; Fig. 8, A-C; and Table 3). Although the changes in association between the NPCs and LB2 fibers were minimal, the differences were statistically significant, with NUP153 KD having the greatest effect.

In contrast, LB2 face center to NPC center distances (-13.6 nm, +0.9 nm, and -18.2 nm vs. scrambled; Observed-Scrambled;  $P < 0.01$ ; Fig. 8, D-F; and Table 4), and the face radii decreased significantly (-16.4 nm, -4.9 nm, -14.8 nm vs. scrambled; Observed-Scrambled;  $P < 0.01$ ; Fig. S9 and Table 5), following KD of TPR, NUP153, or ELYS, respectively. Thus, the main effect of the TPR and ELYS KD was to decrease the LB2 face radii and the distance to the LB2 face centers relative to the NPC distribution. In contrast, the LB2 fiber to NPC center distances were not perturbed to the same extent compared with the other lamin fibers.

#### Silencing of nucleoporins has distinct clustering effects in *Lmna*<sup>-/-</sup> and *Lmnb1*<sup>-/-</sup> MEFs

Thus far, we have seen expansion of faces in the nuclear lamin meshworks along with changes in NPC distribution, number, or density by either knocking out the *Lmna* and *Lmnb1* genes or knocking down the nucleoporin ELYS. To explore whether the phenotypes observed by knocking down the nucleoporins in WT MEFs were dependent on the presence of a lamin isoform, we repeated the siRNA KDs in *Lmna*<sup>-/-</sup> and *Lmnb1*<sup>-/-</sup> MEFs. When we knocked down ELYS in *Lmna*<sup>-/-</sup> and *Lmnb1*<sup>-/-</sup> MEFs, we again observed NPC clustering (Fig. S10 A), although these clusters did not fill the enlarged faces as in WT MEFs. This suggests the clustering effect induced by ELYS depletion is not dependent on the presence of either LA and LC or LB1. When we knocked down NUP153 in *Lmna*<sup>-/-</sup> and *Lmnb1*<sup>-/-</sup> MEFs, we

Table 5. Face radii distributions (fiber to NPC + face to NPC) of WT MEFs with TPR, NUP153, and ELYS KD

siRNA KD	Lamin Labeled	Observed (nm)		Expected (nm)		Observed – expected (nm)		P value vs. expected		Observed – scrambled	P value vs. scrambled	No. of NPCs
		Median	SD	Median	SD	Median	SD	Median	SD	Median (nm)	Median	N
Scrambled	LA	163.3	53.2	171.9	67.4	-8.6	-14.2	0.00				39,096
TPR KD	LA	154.3	49.6	164.3	59.9	-10.0	-10.4	0.00		-9.1	0.00	40,767
NUP153 KD	LA	155.9	48.3	162.8	56.6	-6.9	-8.3	0.00		-7.5	0.00	36,066
ELYS KD	LA	169.7	50.9	168.9	72.3	0.8	-21.3	0.38 <sup>a</sup>	0.00	6.3	0.00	21,521
Scrambled	LC	157.0	50.8	163.3	77.4	-6.4	-26.6	0.00				37,760
TPR KD	LC	150.8	47.0	161.5	103.3	-10.7	-56.2	0.00		-6.2	0.00	35,489
NUP153 KD	LC	152.8	47.3	157.8	58.9	-4.9	-11.7	0.00		-4.1	0.00	39,988
ELYS KD	LC	167.5	52.0	169.0	77.1	-1.5	-25.1	0.00		10.5	0.00	27,053
Scrambled	LB1	174.7	54.7	181.8	92.2	-7.1	-37.5	0.00				37,383
TPR KD	LB1	154.4	48.0	163.2	89.4	-8.9	-41.4	0.00		-20.3	0.00	40,899
NUP153 KD	LB1	173.6	56.1	178.1	67.1	-4.4	-11.0	0.00		-1.1	0.06	31,145
ELYS KD	LB1	157.1	48.8	162.1	70.6	-5.0	-21.7	0.00		-17.6	0.00	24,981
Scrambled	LB2	175.5	52.5	175.0	129.5	0.4	-76.9	0.22 <sup>a</sup>	0.95 <sup>a</sup>			35,444
TPR KD	LB2	159.0	47.7	158.7	147.2	0.3	-99.4	0.16 <sup>a</sup>	0.40 <sup>a</sup>	-16.4	0.00	36,974
NUP153 KD	LB2	170.6	55.2	166.5	68.9	4.0	-13.7	0.00		-4.9	0.00	31,628
ELYS KD	LB2	160.7	48.7	162.7	70.3	-2.0	-21.6	0.00		-14.8	0.00	25,215

Median and SD of the observed and expected sum of lamin fiber and lamin face to NPC distances, the difference between them, P values (see Materials and methods), and number of NPCs. The distributions were also compared with scrambled siRNA controls. The data in each row were collected from 20 cells. The Mann Whitney *U* test and Ansari-Bradley test were used as described in Materials and methods.

<sup>a</sup>P values less than the Bonferroni corrected  $\alpha$  value.

observed clustering of pores (Fig. S10 B), unlike in WT MEFs where we did not observe an NPC clustering phenotype. When we knocked down TPR in *Lmna*<sup>-/-</sup> and *Lmnb1*<sup>-/-</sup> MEFs, we did not note a remarkable phenotype as in WT MEFs.

#### Effect of TPR, ELYS, or NUP153 KD on the number of NPCs

We hypothesized that knocking down nucleoporins may have a similar effect of altering the number of NPCs observed. Compared with WT MEFs, we saw a significant ( $P < 0.001$ ) reduction of NPCs upon ELYS KD but did not see a significant reduction upon TPR KD or NUP153 KD (Fig. S10, C and D). The drop in NPC numbers upon ELYS KD may be due to our inability to resolve individual NPCs in clusters. Due to reports of an increase in NPC number upon TPR KD (McCloskey et al., 2018), we further analyzed whether we observed changes in TPR KD in *Lmna*<sup>-/-</sup> or *Lmnb1*<sup>-/-</sup> MEFs (Fig. S10 D). We did not observe a significant change in NPC number in WT, *Lmna*<sup>-/-</sup>, or *Lmnb1*<sup>-/-</sup> MEFs. Only ELYS KD had a significant effect on reducing the number of NPCs, while NUP153 KD and TPR KD did not have a significant effect.

## Discussion

Ever since the first descriptions of the NE as a distinct structure in eukaryotic cells, the relationships between the components of the structure have been the subject of intense scrutiny. However, due to multiple factors, including its dense composition,

relative insolubility, and thin structure sandwiched between the chromatin and the cytoplasm, determination of its fine structure has been elusive. Several lines of evidence support the consensus that NPCs are anchored to the lamina during interphase. Studies of the dynamics of both lamins and NPCs in interphase cells show that neither has appreciable lateral mobility in the NE (Moir et al., 2000; Daigle et al., 2001). Biochemical fractionation of the NE as well as electron microscopy studies of both somatic cells and amphibian eggs demonstrated that lamins and NPCs are intimately associated (Dwyer and Blobel, 1976; Gerace et al., 1984; Scheer et al., 1976).

Our 3D-SIM imaging and quantitative analysis of the MEF nuclei constitute a dataset that reveals important insights into the structural relationships between the lamin fibers and NPCs. Our study uses indirect immunofluorescence to robustly label structures in situ with fluorescent labels and provides sufficient labeling accuracy for the resolution of 3D-SIM to localize the structures at the scale of interest. While smaller labeling complexes do exist (Carrington et al., 2019), these do not provide significant advantages for the resolution limits of 3D-SIM. Our image analysis focuses on localizing structures, lamin fibers, and NPCs, to high precision and then performing statistical analysis on the aggregate dataset. This is distinct from localizing individual fluorophores through single-molecule localization microscopy (SMLM), the Delaunay triangulation of those fluorophore localizations, or subgraphs of the Delaunay triangulation such as the Euclidean Minimum Spanning Tree (Xie et al.,

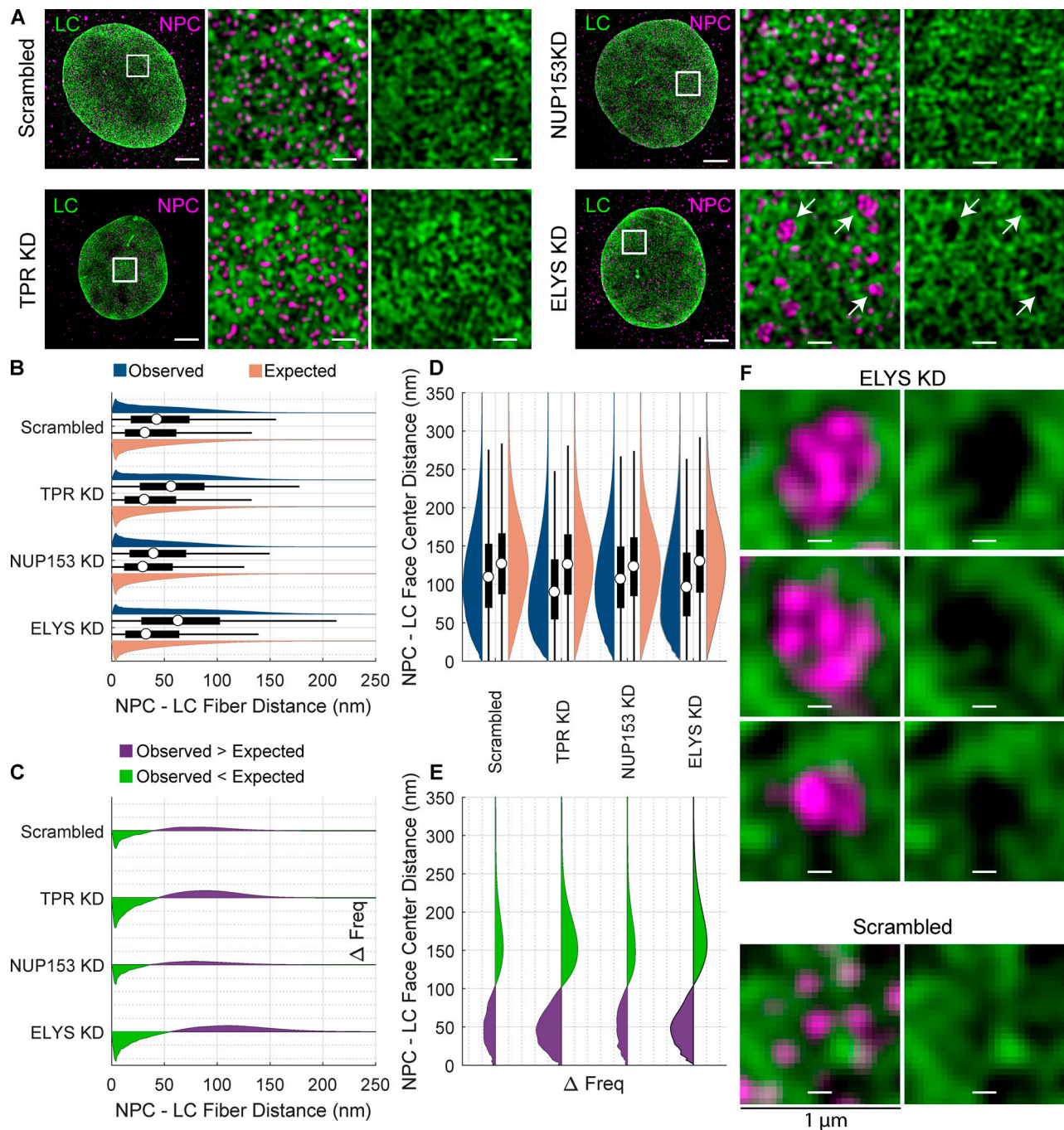
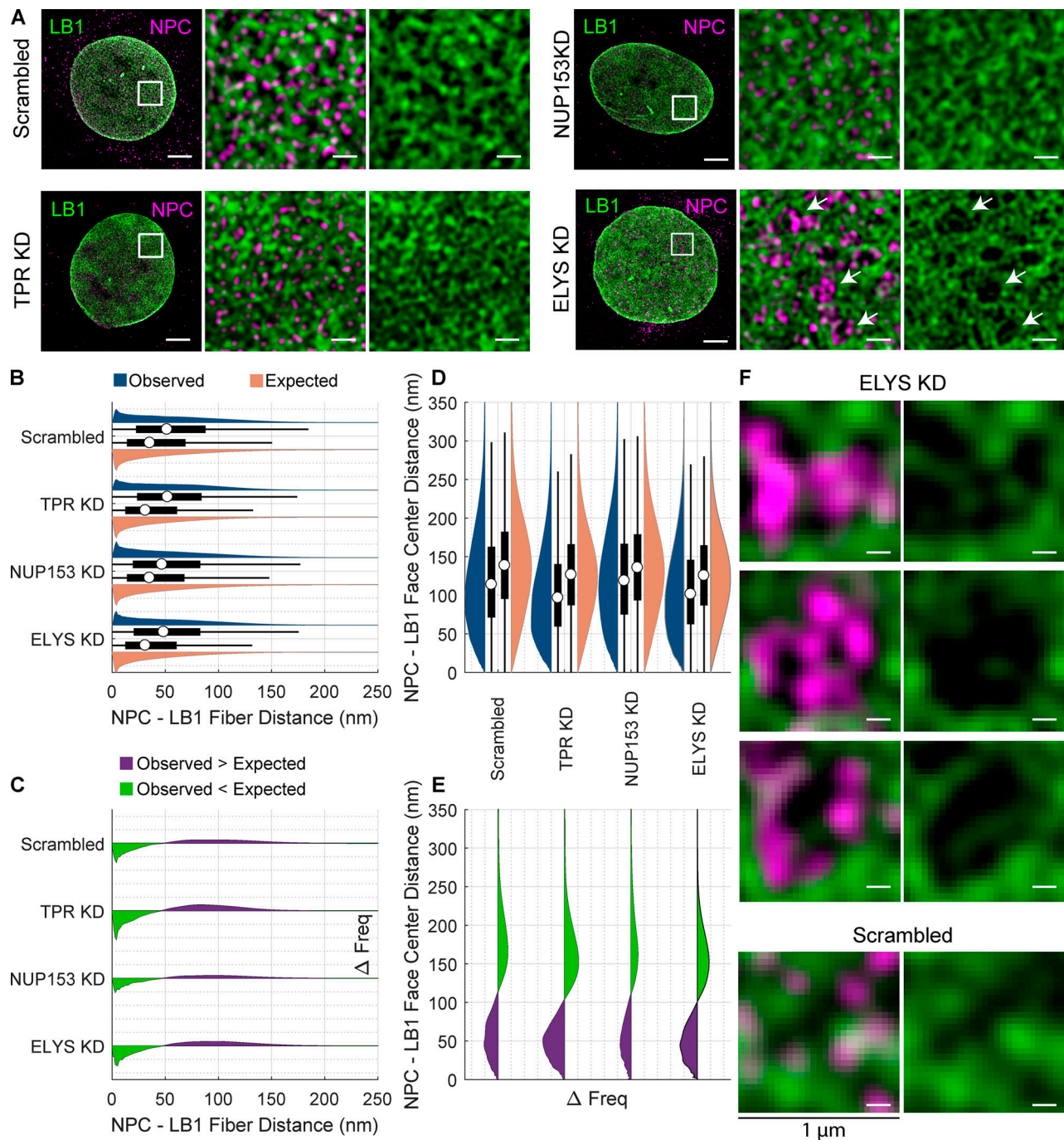
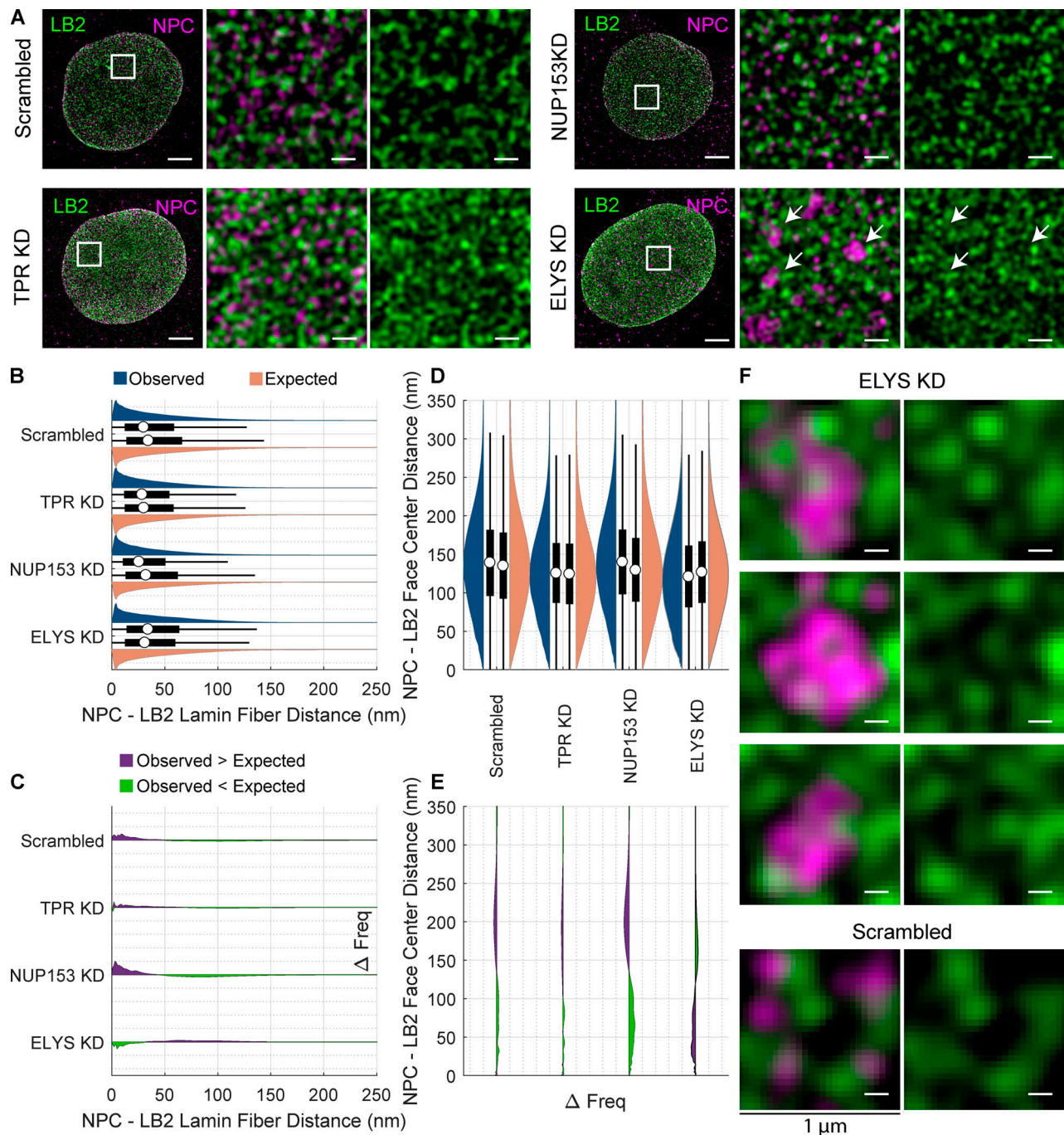


Figure 6. **Co-distribution of LC and NPC components after siRNA transfection shows enlarged LC meshwork filled with NPC clusters upon ELYS KD.** (A) Double-label immunofluorescence images of LC (green) and NPCs (magenta) following KDs of TPR, NUP153, ELYS, and scramble control. Area of white box (left) is shown merged (center) and just lamin (right). White arrows indicate areas of NPC clustering. Scale bar = 5 μm (full), 625 nm (inset). (B) Paired violin and box plots of NPC center to LC fiber center distances. The violin (blue) and box plots on top represent the observed distance distributions. The violin (red) and box plots on bottom represent the expected distance distributions under the null hypothesis. The white circle indicates the median. The thick black bar indicates the interquartile range (IQR). The black whiskers indicate 1.5 times the IQR. (C) Frequency (Freq) difference plots of observed minus expected LC fiber to NPC distances for the KD series. The green portion below the line indicates where the observed frequency is less than expected. The purple portion above the line indicates where the observed frequency is greater than expected. (D) NPC center to LC face center distances displayed as in B, rotated 90° counterclockwise. (E) Frequency difference plot of NPC center to LC face center distances, displayed as in C, rotated 90° counterclockwise. (F) 1-μm<sup>2</sup> areas around NPC clusters formed after scramble treatment or ELYS KD indicated by white arrows in A shown merged (left) and just lamin (right). Each violin or box plot represents 20 cells with the number of NPCs detailed in Table 3. Scale bar = 150 nm.



**Figure 7. Co-distribution of LB1 and NPCs after siRNA transfection reveals LB1 fibers within NPC clusters upon ELYS KD.** **(A)** Double-label immunofluorescence images of LB1 (green) and NPCs (magenta) following KDs of TPR, NUP153, ELYS, and scramble control. Area of white box (left) is shown merged (center) and just lamin (right). White arrows indicate areas of NPC clustering. Scale bar = 5  $\mu\text{m}$  (full), 625 nm (inset). **(B)** Paired violin and box plots of NPC center to LB1 fiber center distances. The violin (blue) and box plots on top represent the observed distance distributions. The violin (red) and box plots on bottom represent the expected distance distributions under the null hypothesis. The white circle indicates the median. The thick black bar indicates the interquartile range (IQR). The black whiskers indicate 1.5 times the IQR. **(C)** Frequency (Freq) difference plot of observed minus expected LB1 fiber to NPC center distances for the KD series. The green portion below the line indicates where the observed frequency is less than expected. The purple portion above the line indicates where the observed frequency is greater than expected. **(D)** NPC center to LB1 face center distances displayed as in B, rotated 90° counterclockwise. **(E)** Frequency (Freq) difference plot of NPC to LB1 face center distances, displayed as in C, rotated 90° counterclockwise. **(F)** 1- $\mu\text{m}^2$  areas around NPC clusters formed after scramble treatment or ELYS KD indicated by white arrows in A shown merged (left) and just lamin (right). Each violin or box plot represents 20 cells with the number of NPCs detailed in Table 3. Scale bar = 150 nm.



**Figure 8. Co-distribution of LB2 and NPCs after siRNA transfection does not show enlarged faces around NPC clusters upon ELYS KD.** (A) Immunofluorescence images of LB2 (green) and NPCs (magenta) following KDs of TPR, NUP153, ELYS, and scramble control. Area of white box (left) is shown merged (center) and just lamin (right). White arrows indicate areas of NPC clustering. Scale bar = 5  $\mu$ m (full), 625 nm (inset). (B) Paired violin and box plots of NPC center to LB2 fiber center distances. The violin (blue) and box plots on top represent the observed distance distributions. The violin (red) and box plots on bottom represent the expected distance distributions under the null hypothesis. The white circle indicates the median. The thick black bar indicates the interquartile range (IQR). The black whiskers indicate 1.5 times the IQR. (C) Frequency (Freq) difference plot of observed minus expected LB2 fiber center to NPC center distances. The green portion below the line indicates where the observed frequency is less than expected. The purple portion above the line indicates where the observed frequency is greater than expected. (D) NPC center to LB2 face center distances displayed as in B, rotated 90° counterclockwise. (E) Frequency difference plot of NPC to LB2 face center distances, displayed as in C, rotated 90° counterclockwise. (F) 1- $\mu$ m<sup>2</sup> areas around NPC clusters formed after scramble treatment or ELYS KD indicated by white arrows in A shown merged (left) and just lamin (right). Each violin or box plot represents 20 cells with the number of NPCs detailed in Table 3. Scale bar = 150 nm.

2016; Kittisopikul et al., 2019). Extracting information about fibrous lamin structures from SMLM data would require additional analysis not directly realizable from SMLM localizations or their graphs (Peters et al., 2018; Kittisopikul et al., 2019). Our analysis of lamin fibers as employed here has been purpose built and validated for use in dense structures such as lamin meshworks with complex junctions (Kittisopikul et al., 2020). Electron microscopy as well as the meshwork-altering perturbations produced here suggest the fibrous nature of lamins exists even in the dense WT lamina. To evaluate the relationship between lamin fibers and NPCs to high precision, we have exploited the continuous nature of the imaging dataset afforded by Nyquist sampling to localize structures by mathematical optimization as described in Materials and methods. The combination of super-resolution microscopy and computational analysis as a dataset will allow researchers to pursue further questions about the relationship of lamin fibers and NPCs as we have demonstrated here.

Which of the lamin isoforms interact with the NPCs has been a relevant question, since the four major lamin isoforms, LA, LC, LBI, and LB2, are not all expressed throughout development and each may not be expressed in all cell types (Burke and Stewart, 2014). With the aid of super-resolution microscopy techniques, it is now established that each of the lamin isoforms assembles into a distinct network in the NE (Shimi et al., 2015; Xie et al., 2016), and the relationship of NPCs with each lamin isoform can be determined with increasing precision. NPCs assemble on chromatin during NE reassembly after mitosis, and new NPCs continue to be integrated into the NE throughout interphase (Otsuka and Ellenberg, 2018). Studies on the cell cycle-dependent dynamics of NPCs have identified so-called “pore-free islands” in G1 nuclei of multiple cell types (Maeshima et al., 2006; Mimura et al., 2017). These pore-free areas are enriched in LA/LC and generally devoid of B-type lamins. Ectopic overexpression of LA induces the formation of pore-free islands while depletion of LA/LC by siRNA KD dispersed pore-free islands, leading to a more uniform distribution of NPCs (Maeshima et al., 2006). The expression of any of several laminopathic forms of LA/LC or depletion of LBI leads to the formation of herniations or blebs in the NE that contain an expanded LA/LC meshwork and are generally depleted in B-type lamins (Goldman et al., 2004; Shimi and Pflieger, 2008; Mounkes et al., 2003; Raharjo et al., 2001). These blebs are also deficient in NPCs. Together, these studies suggest that B-type lamins may be more important than LA/LC for the normal distribution of NPCs in the NE. This conclusion makes sense intuitively, since stem cells and some differentiated cells express very little or no LA/LC, yet have what appears to be a regular distribution of NPCs (Burke and Stewart, 2014). However, other studies have suggested that lamin isoforms can function redundantly to ensure normal NPC distribution (Guo et al., 2014). Our findings presented here support the notion that both LA and LBI have clear spatial relationships with NPCs, and these relationships are preserved when either LA/LC or LBI is absent. Although the proximal lateral relationship between NPCs and LA and LBI fibers is retained in both types of lamin null cells, the quantitative data suggest that the presence of LA fibers may be

more important to the LBI-NPC relationship than the presence of LBI fibers are to the LA-NPC relationship. Our work builds upon prior cryo-ET studies (Mahamid et al., 2016; Turgay et al., 2017; Tatli and Medalia, 2018) by directly examining specific distances and contacts between lamin isoforms and NPCs. Using cryo-ET, we were able to demonstrate that both LA and LBI fibers lie in close proximity to the NPC and, in several cases, can be seen in intimate association with the nucleoplasmic ring structure of the NPC. This finding supports our super-resolution results that indicate a close physical relationship for both LA and LBI with NPCs over the entire nucleus. Measurement of LC interactions with NPCs followed a similar trend to those of LA and LBI in our analyses, although we could not draw firm conclusions on the LC-NPC interaction due to the small magnitude of the observed values relative to expected. Surprisingly, we did not find an obvious relationship between LB2 and NPCs in our analysis.

Xie et al. (2016) previously performed super-resolution microscopy studies of the relationships between lamins and NPCs in mouse adult fibroblasts. By reexpressing mEOS-tagged LA or LC in *Lmna*<sup>-/-</sup> cells, they found NPCs concentrated in the spaces between LA fibers and a close association of NPCs with the LC networks. These findings seem to oppose those we report here. There are several possible explanations for these discrepancies including (1) possible differences between adult fibroblasts and embryonic fibroblasts, (2) possible differences in an ectopically expressed lamin network versus the endogenous networks, and (3) overexpression of LA only or LC only versus cells expressing all four lamin isoforms in the natural ratio. The results could be reconciled if LC fibers are in close contact with NPCs but do not significantly influence their position. Our study examines co-distribution in space and not merely spatial proximity by comparing expected and observed distributions. We regard association as distinct from proximity. Further studies will be necessary to address these differences in results.

Our results also provide new and important insights into lamin-NPC interaction by knocking down specific nucleoporin levels using siRNA for ELYS, TPR, or NUP153. The KD occurred over the course of 96 h, and thus a limitation of our study is that our observations are of cells that may have adapted to extended depletion of these nucleoporins. Each KD had unique effects on both NPC distribution and lamin meshwork structure. ELYS KD caused dramatic changes in NPC distribution attributable to NPCs clustering within the open faces formed by all of the lamin meshworks and a reduction in NPC number. Depletion of ELYS also led to an increase in the lamin fiber to NPC distance for LA, LC, and LB2 but a decrease in the LBI to NPC distance. NPCs form in a biphasic pattern, at the end of mitosis as the NE reforms and then during interphase (Doucet et al., 2010). These two processes differ in the order that nucleoporins assemble and in the enzymatic requirements for assembly. The postmitotic phase involves the recruitment of the NUP107-160 subcomplex to the chromatin surface by the binding of one component of the complex, ELYS/MEL-28, to nucleosomes (Rasala et al., 2006; Galy et al., 2006; Gómez-Saldivar et al., 2016). While we have not demonstrated a direct interaction between ELYS and the lamins, it is clear that the presence of ELYS is required to maintain

lamin-NPC interactions. The clustering of NPCs after ELYS KD is likely due to the failure of NPCs to correctly assemble on chromatin following mitosis, suggesting that, at least for NPCs formed at NE reformation, their association with lamins occurs at that time. ELYS KD has previously been shown to decrease NPC density (Doucet et al., 2010; Jevtić et al., 2019; Mimura et al., 2016), disrupt the proper localization of the integral inner nuclear membrane protein lamin B receptor (Mimura et al., 2016), and cause the cytoplasmic accumulation of LB1 (Jevtić et al., 2019; Mimura et al., 2016). However, these previous studies did not find clustering of NPCs or changes in lamin meshwork structure.

TPR is a nucleoporin located in the nuclear basket structure of the NPC and could act as a negative regulator of NPC number (McCloskey et al., 2018). In contrast, two other studies found that siRNA reduction of TPR reduced NPC number (Funasaka et al., 2012; Fišerová et al., 2019). In our experiments, we also observed a small statistically insignificant increase in NPC numbers after TPR KD in WT cells. When we depleted TPR in *Lmna*<sup>-/-</sup> and *Lmnb1*<sup>-/-</sup> cells, a similar small, statistically insignificant increase in NPCs was observed, suggesting that neither lamin isoform alone is involved in regulating NPC numbers. As with ELYS KD, TPR KD resulted in displacement of the NPCs away from the lamin fibers, with the exception of LB2 fibers, which were slightly closer to the NPCs when TPR was depleted. NUP153 depletion had the most consistent effects on the lamin fiber-NPC relationship with a decrease in lamin fiber to NPC distance and a compaction of the lamin meshworks, although these changes were more modest than those of the other nucleoporin KDs. Surprisingly, KD of NUP153 in *Lmna*<sup>-/-</sup> and *Lmnb1*<sup>-/-</sup> cells led to clustering of NPCs in the lamin meshwork faces. This suggests that an interaction of NUP153 with both lamin isoforms is required for normal NPC distribution. NUP153 is known to bind to both LA and LB1 (Al-Haboubi et al., 2011).

The results presented here suggest that the lamina structure and NPCs are codependent; that is, changing one of the structures has an effect on the other's distribution. In addition to the NPC clustering in lamin meshwork faces after ELYS reduction, the lamin meshworks became larger for LA and LC but became smaller for LB1 and LB2. In contrast, KD of either TPR or NUP153 caused each of the lamin meshwork faces to decrease in size. Based on these results, it is tempting to speculate that number and structural composition of NPCs helps to determine lamin meshwork structure. Our results show that each of the lamin isoforms appears to interact differently with the three nucleoporins. It should be noted that while ELYS is required for postmitotic NPC assembly (Franz et al., 2007), NUP153 is required for interphase NPC assembly (Vollmer et al., 2015; Franz et al., 2007), whereas TPR is required only for formation of the nuclear basket (Duhéron et al., 2014). In cell-free extracts of *Xenopus laevis* eggs that recapitulate nuclear assembly, the recruitment of NUP153 to the NE is dependent on the formation of the lamina (Smythe et al., 2000). TPR is also required to maintain the heterochromatin exclusion zones found at the NPCs (Krull et al., 2010), and all three nucleoporins are known to affect chromatin modification states (Kuhn and Capelson, 2019). The lamins are also closely associated with chromatin at

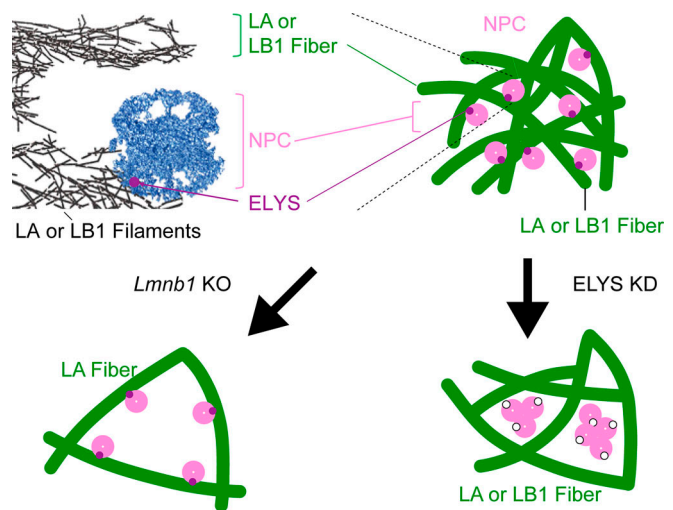


**Figure 9. Schema of lamin-NPC interactions.** Top left: structure of LA or LB1 fibers consisting of individual filaments and an NPC as seen by cryo-ET. Top right: NPCs associating next to LA or LB1 fibers at the resolution of structured illumination light microscopy. Bottom left: knocking out LB1 results in enlarged faces where NPCs adhere to LA fibers. Bottom right: knocking down ELYS results in enlarged faces containing clusters of NPCs missing ELYS (see Discussion).

the nuclear periphery, and it is likely that peripheral chromatin is also playing a role in mediating the association of lamins and NPCs and their distribution in the NE, in particular during postmitotic NE assembly.

Overall, the extensive SIM imaging and quantitative analysis performed here provide important biological insight as to how NPCs and lamin fibers are arranged in the mammalian nucleus. In perturbing the cells and their nuclei by either knocking out lamin isoforms, LA/LC or LB1, or knocking down nucleoporins, our dataset provides knowledge about interactions mediated by these specific lamin isoforms and nucleoporins. In particular, it is clear from this dataset that knocking down lamin isoforms results in a change in the spatial distribution of NPCs. Additionally, knocking down nucleoporins has an effect on the spatial distribution of the lamin fiber meshwork. Specifically, among other findings, NPCs are positioned next to LA and LB1 fibers in an ELYS-dependent manner, and removing any of these components in whole or in part changes how the remaining components are distributed (Fig. 9). Therefore, the lamins and NPCs play a role in organizing each other at the nuclear periphery.

## Materials and methods

### Sample size estimation

The initial light microscopy images of WT, the lamin KO cells, and the cryo-ET data were acquired before the design of the study and before the computational analysis was developed. Hierarchical power analysis was performed for the siRNA KD series of experiments based upon the effect sizes observed in the initial light microscopy images. We sought to evaluate changes in distance between lamin and NPCs as well as changes in NPC number. The limiting factor was the number of cells that needed

to be observed in order to detect a  $\pm 20\%$  change in number of NPCs per cell with a power of 0.8 at an  $\alpha$  of 0.01 with the Mann-Whitney *U* test. The *wmwpow* package (Mollan et al., 2020) in R (R Core Team, 2020) was used. Using the estimation methods in that package, it was determined that imaging 20 cells would exceed those requirements. Based on thousands of distances being measured per cell, it was determined that the power of the lamin-NPC distance studies would also exceed the requirements.

### Replicates

Each experiment was performed in duplicate as technical replicates. Each technical replicate was performed at a distinct time and included all steps from cell culture to fixation and staining. Additionally, for each technical replicate, two sets of coverslips were produced. In Table 1 and Table 2, 10 cells were evaluated per row. In Table 3, Table 4, and Table 5, 20 cells were evaluated per row. The cells were distributed across the four coverslips produced. Outliers were not excluded from the data. Microscopy as described below was done on fixed samples in blocks of time using coverslips from multiple technical replicates. Experimental samples and their controls were conducted within the same microscopy session.

### Statistical reporting

Statistical analysis was done in MATLAB (Mathworks) other than the power calculation done in R as noted above. The frequency of the simulated distances was compared with the observed distances using the Mann-Whitney *U* test, also known as the Wilcoxon rank sum test. A nonparametric test was used since the Kolmogorov-Smirnov test rejected the null hypothesis that the distributions were normal.

The Mann-Whitney *U* test evaluated the null hypothesis that the two sets of samples (observed vs. expected, ELYS siRNA vs. scrambled siRNA, etc.) were drawn from the same distribution. If the Mann-Whitney *U* test failed to reject the null hypothesis for the distance measurements, the Ansari-Bradley test was applied to examine the null hypothesis that the dispersions (i.e., the SD) of the distributions were the same. Bonferroni corrections were applied to the  $\alpha$  value to compensate for multiple comparisons by dividing an  $\alpha$  value of 0.05 by the number of comparisons in the table or figure.

### Cell culture

Immortalized WT, *Lmna*<sup>-/-</sup>, *Lmnb1*<sup>-/-</sup>, and *Lmnb2*<sup>-/-</sup> MEFs were cultured as previously described (Shimi et al., 2015). Briefly, cells were cultured in modified DMEM (Thermo Fisher Scientific) supplemented with 10% fetal calf serum, 50 U/ml penicillin G, and 50  $\mu$ g/ml streptomycin sulfate (Thermo Fisher Scientific) at 37°C in a humidified CO<sub>2</sub> incubator.

### Super-resolution microscopy

3D-SIM was performed as previously described (Shimi et al., 2015). Briefly, a Nikon Structured Illumination Super-resolution Microscope System (N-SIM) was built on an ECLIPSE Ti-E (Nikon) equipped with a scientific complementary metal-oxide-semiconductor (sCMOS) camera ORCA-Flash 4.0 (Hamamatsu Photonics Co.) and an oil immersion objective

lens CFI SR (Apochromat TIRF 100 $\times$ , NA = 1.49, Oil, WD = 0.12; Nikon). N-SIM was operated with NIS-Elements AR (Nikon). All imaging was conducted at room temperature. For image acquisition, 21 optical sections including a region of the lamina were taken at 50-nm intervals. For image reconstruction from the raw data, illumination modulation contrast, high-resolution noise suppression, and out-of-focus blur suppression were set with fixed values of 1, 0.75, and 0.25, respectively. For presentation, images were adjusted for brightness and contrast.

### Indirect immunofluorescence

Samples for indirect immunofluorescence were processed as previously described (Shimi et al., 2015). Cells were seeded on Gold Seal coverglasses (22  $\times$  22 mm<sup>2</sup>, no. 1.5; Thermo Fisher Scientific) and fixed with methanol for 10 min at -20°C. Lamins were stained with rabbit polyclonal anti-LA (1:500; 323; Dechat et al., 2007), goat polyclonal anti-LB1 (1:500; SC-6217; Santa Cruz Biotechnology) and rabbit monoclonal LB2 (1:100; EPR9701(B); Abcam), and rabbit polyclonal anti-LC (1:500; 321; Kochin et al., 2014). The LC antibody (321) was made in rabbits with a synthetic peptide (CHHVSGSRR) conjugated to Keyhole Limpet hemocyanin and validated as described below (Fig. S5). Nucleoporins were stained with mouse monoclonal MAb414 (1:1,000; BioLegend; Table 6). The secondary antibodies used were donkey anti-mouse IgG-Alexa Fluor 488, donkey anti-mouse IgG-Alexa Fluor 568, donkey anti-rabbit IgG-Alexa Fluor 488, donkey anti-rabbit IgG-Alexa Fluor 568, donkey anti-goat IgG-Alexa Fluor 488, and donkey anti-goat IgG-Alexa Fluor 568 (all 1:500; Thermo Fisher Scientific). Processed coverslips were mounted with ProLong Diamond antifade reagent (P36961; Thermo Fisher Scientific).

### Validation of primary anti-LC (323) specificity

Whole cell lysates of WT MEFs in Laemmli sample buffer were resolved by SDS-PAGE (6  $\times$  10<sup>4</sup> cells/lane) and transferred to nitrocellulose, and lanes were cut into individual strips. After blocking in 5% nonfat milk dissolved in TBS with 0.1% Tween 20 for 1 h, the blots were probed overnight at 4°C with mixing. The dilutions of each antiserum were anti-LA/LC (266) 1:1,000 (Butin-Israeli, 2011); anti-LC (321) 1:500; and anti-LA (323) 1:1,000 (Table 7). After washing 3 $\times$  with TBS with 0.1% Tween 20 for 5 min each at room temperature, the blots were probed with a 1:15,000 dilution of anti-rabbit secondary antibody (LI-COR IRDye 800CW) for 45 min at room temperature. The blots were then washed as before and allowed to dry before imaging with an Odyssey Fc at 800 nm (Fig. S5).

### RNA interference

ON-TARGETplus siRNA oligos (Dharmacon) were used for RNAi-mediated KD experiments. Scrambled sequence for control siRNAs: (D-001810-01) 5'-UGGUUUACAUGUCGACUAA-3'; (D-001810-02) 5'-UGGUUUACAUGUUGUGUGA-3'; (D-001810-03) 5'-UGGUUUACAUGUUUUCUGA-3'; (D-001810-04) 5'-UGGUUUACAUGUUUCCUA-3'. *NUP153* siRNAs: (J-057025-11) 5'-CGCUAUGUGCAUUGAUAAA-3'; (J-057025-12) 5'-GGGACAGGC UUUGGAGAUAA-3'. *ELYS* siRNA: (J-051465-09) 5'-CCACUGAAC UAACUACUAA-3'; (J-051465-10) 5'-GGAAGAAGAAGGACGUU

Table 6. Primary antibodies used for immunofluorescence

Target	Antibody	Catalog no.	Supplier	Host species	Dilution
LA	323	<a href="#">Dechat et al. (2007)</a>	Goldman Lab	Rabbit	1/500
LC	321	<a href="#">Kochin et al. (2014)</a>	Goldman Lab	Rabbit	1/500
LB1	M20	sc-6217	Santa Cruz	Goat	1/500
LB2	EPR9701(B)	ab151735	Abcam	Rabbit	1/100
FXFG Repeat Nups	mAb414	902902	BioLegend	Mouse	1/1,000

A-3'. TPR siRNA: (J-041152-09) 5'-CAACAAACAUCUACGGUA-3'; (J-041152-10) 5'-CGUGACAUGUACCGAAUUU-3'.

$5 \times 10^4$  MEFs were plated into each well of 6-well plates 24 h before transfection. 30 pmol of siRNA oligos was transfected onto the cells in each well with Lipofectamine RNAiMAX transfection reagents (Thermo Fisher Scientific), following the manufacturer's instructions. 48 h after incubation at 37°C, the transfected cells were trypsinized and replated at  $5 \times 10^4$  cells/well into each well of 6-well plates and transfected with 30 pmol of the siRNA. 48 h after incubation at 37°C, the transfected cells were trypsinized and replated on coverslips for indirect immunofluorescence or plated into a 60-mm dish for Western blotting.

#### Quantitative blotting of anti-nucleoporin antibodies

The linearity of antibodies to nucleoporins was determined by immunoblotting of whole cell lysates of WT MEFs. Five samples of MEF lysates containing between  $7.5 \times 10^3$  and  $9 \times 10^3$  cells were separated in duplicate lanes of a 7.5% SDS-polyacrylamide gel (SDS-PAGE) and transferred to nitrocellulose for immunoblotting. After transfer, the membrane was briefly rinsed in dH<sub>2</sub>O and stained with Revert Protein Stain (LI-COR) and imaged in an Odyssey Fc (LI-COR) at 700 nm. The membrane was then washed with TBS and blocked in 5% nonfat dry milk in TBS for 1 h at room temperature and then in the same solution containing 0.1% Tween 20 for 30 min. For incubation with antibodies, the appropriate antibody was diluted in blocking solution with Tween at the indicated concentration (see [Table 8](#)) and incubated overnight at 4°C with gentle agitation. The blots were washed three times for 5 min each with TBS containing 0.1% Tween 20. For detection, the appropriate secondary antibodies (LI-COR IRDye 800CW) were diluted 1:15,000 in 5% nonfat dry milk containing 0.2% Tween 20 and incubated with the membrane for 1 h at room temperature with gentle agitation. The membranes were washed 3× 5 min each with TBS containing 0.1% Tween 20 and allowed to dry. The dried membranes were imaged in an Odyssey Fc at 800 nm.

Images of the total protein stain and specific antibody labeling were analyzed using Empiria Studio Software (LI-COR

Biosciences). The intensity of the specific antibody labeling in each lane was corrected for protein load using the software, and the linearity of the antibody response was determined by the software.

The degree of KD for each nucleoporin was determined by SDS-PAGE by loading duplicate samples of each KD cell lysate such that the antibody response should be in a linear range based on the analysis of WT lysates. For quantitation of KD, a dilution series of WT lysate was run on the same gel at concentrations that were expected to be in the linear range of the antibody response. After electrophoresis and transfer, the membranes were treated identically to the conditions for determining antibody linearity and imaged in the Odyssey Fc, and the images were analyzed using Empiria software.

#### NPC-lamin rendered view

Cryo-electron tomograms that were acquired previously ([Turgay et al., 2017](#)) were further analyzed. The central coordinates of NPCs within cryo-tomograms of NE were determined manually, and subtomograms (340 nm × 340 nm × 20 nm) were reconstructed in MATLAB using the TOM toolbox ([Nickell et al., 2005](#)). The lamin filaments and NPCs in four selected subvolumes were segmented manually and rendered using the Amira software package (Thermo Fisher Scientific).

#### Immunogold labeling image processing

Subtomograms of gold-labeled lamins ([Turgay et al., 2017](#)) were reconstructed as described above (47 subtomograms). The subvolumes containing NPCs (in top-view orientation) were projected along the Z axis, to produce a 2D image. The coordinates of the gold clusters (6 nm and 10 nm) were identified manually and counted. The respective histograms were drawn in Excel (Microsoft).

#### Computational image analysis

Computational image analysis was done using MATLAB custom software developed in the Jaqaman Lab. Nikon ND2 files

Table 7. Antibodies used for Western blotting to evaluate anti-LC (321) specificity

Target	Antibody	Catalog no.	Supplier	Host species	Dilution
LA	323	<a href="#">Dechat et al. (2007)</a>	Goldman Lab	Rabbit	1/1,000
LC	321	<a href="#">Kochin et al. (2014)</a>	Goldman Lab	Rabbit	1/500
LA/LC	266	<a href="#">Butin-Israeli (2011)</a>	Goldman Lab	Rabbit	1/1,000

Table 8. **Antibodies used for Western blotting to determine nucleoporin KD efficiency**

Target	Antibody	Catalog no.	Supplier	Host species	Concentration
NUP153	R3G1	sc-101544	Santa Cruz	Rat	1 $\mu\text{g ml}^{-1}$
ELYS	bs-9880R	bs-9880R	Bioss	Rabbit	0.1 $\mu\text{g ml}^{-1}$
TPR	ab84516	ab84516	Abcam	Rabbit	0.2 $\mu\text{g ml}^{-1}$

containing image and metadata were loaded into MATLAB using Bioformats (Open Microscopy Environment; [Linkert et al. \[2010\]](#)). NPCs were detected and localized using an adapted point Source Detector routine from the laboratory of Gaudenz Danuser, which involved 2D local maxima detection, Gaussian fitting, and Gaussian mixture modeling. Lamin fibers were segmented using multi-orientation analysis as described in [Kittisopikul et al. \(2020\)](#) to accurately segment a meshwork structure with many junctions. Lamin fibers were further localized as described below. The source is available at <http://doi.org/10.5281/zenodo.4504194>. Computation was conducted on Northwestern University's high-performance computing environment, Quest. Files were stored on Northwestern University Research Data Storage Service FSMRES-FILES. Globus.org and Box.com were used to transfer files between storage and computational environments.

#### Expected distribution of NPCs

In this study, the null hypothesis is that there is no relationship between the position of lamin fibers and NPCs within the nucleus. To determine if a relationship or an association between lamin fibers and NPCs exists, we used statistical methods to see if the observed distances between lamin fibers and NPCs were significantly different than what would be expected under this null hypothesis.

To calculate the expected distribution of NPCs relative to the lamin fibers for each nucleus under that null hypothesis, we used a Monte Carlo simulation to randomly place NPCs within the nucleus. 60,000 pseudorandom pairs of numbers representing XY locations of NPCs were selected within the image. If they were not within the mask of the nucleus represented by a complex hull, then the XY locations were rejected. The distance between the remaining XY locations were measured to the nearest lamin fiber location as determined below. The initial number of pairs was selected empirically such that the distance frequencies would not fluctuate more than 1% for 10-nm bins.

#### Localization of lamin fibers in orientation space

To localize lamin fibers, we used an image analysis algorithm that we previously developed that involves the construction of a 3D orientation space by augmenting a 2D image with orientation as an additional third dimension ([Kittisopikul et al., 2020](#)). There, we focused on addressing the continuous nature of the orientation dimension; we left the spatial dimensions discretely sampled and localized line detections to the nearest pixel in the Non-Maximum Suppression and Non-Local Maxima Suppression procedures.

Here, we extend the procedure by using the orientations to localize lines, the lamin fibers, to subpixel precision by also

treating the spatial dimensions as continuous. Given sufficient signal-to-noise ratios and sampling in excess of that required by the Nyquist-Shannon-Whittaker-Kotelnikov sampling theorem, the spatial dimension could also be treated continuously through interpolation. In particular, we used spline interpolation ([Unser, 1999](#)). In that case, we can state the localization problem as solving a system of partial differential equations where  $R(x, y, \theta; K)$  is the steerable filter response at some location  $(x, y)$  at orientation  $\theta$  at the orientation-resolution  $K$ .

For  $\vec{v} = (\cos(\phi), \sin(\phi))$ , we want all  $(x, y, \phi)$  such that

$$\begin{aligned} \frac{\partial R(x, y, \phi; K_1)}{\partial \phi} &= 0, \quad \frac{\partial^2 R(x, y, \phi; K_1)}{\partial \phi^2} < 0 \\ \frac{\partial R(x, y, \phi; K_2)}{\partial \vec{v}} &= 0 = \frac{\partial R(x, y, \phi; K_2)}{\partial x} \cos(\phi) \\ &+ \frac{\partial R(x, y, \phi; K_2)}{\partial y} \sin(\phi) \\ \frac{\partial^2 R(x, y, \phi; K_2)}{\partial \vec{v}^2} &= \frac{\partial^2 R(x, y, \phi; K_2)}{\partial x^2} \cos^2(\phi) \\ &+ 2 \frac{\partial^2 R(x, y, \phi; K_2)}{\partial x \partial y} \cos(\phi) \sin(\phi) \\ &+ \frac{\partial^2 R(x, y, \phi; K_2)}{\partial y^2} \sin^2(\phi) < 0. \end{aligned}$$

$\vec{v}$  is a vector normal to the structure being localized. As explained in [Kittisopikul et al. \(2020\)](#),  $K_1$  and  $K_2$  may differ since the orientation resolution used for orientation detection may differ from the orientation resolution used to localize the detection in space.

#### Localization of lamin meshwork face centers

To understand the relationship of NPCs to the lamin structure, we also measured the distance of the NPCs from their "centers," which we defined as the points farthest away from the lamins within a local neighborhood.

Face centers were localized by identifying local maxima of the distance transform relative to the lamin fibers. A 2D disc with a 5-pixel radius (150 nm) was used as a structuring element with morphological dilation. This identified the maximum distance within a disc centered at each pixel. The local maxima were detected at the points when the maximum distance within the disc coincided with an identical distance assigned to that pixel via the distance transform. When a connected region with points equidistant from the lamin fibers was found, the centroid of that region was selected as the face center.

Because faces are not always convex or there may be lamin fibers protruding into faces, multiple distinct centers may be detected. In this case, the distance from the NPC is measured to the nearest face center.

## Online supplemental material

The supplemental material consists of 10 supplemental figures. These include bivariate histograms, violin plots of the numbers of NPCs, Western blots, and additional images of siRNA KD of ELYS, NUP153, and TPR in *Lmnb1*<sup>-/-</sup> MEFs. The bivariate distributions are shown since the distance of the NPC to the lamin fiber and to the face center may be related. In particular, the bivariate distance histograms show distinct green (observed less than expected) and purple (observed more than expected) areas, indicating the difference between observed and expected is due to correlated changes in both distance measures.

Fig. S1 contains bivariate histograms of LA fiber–NPC and face center–NPC distances in single nuclei and illustration of distances. Fig. S2 contains bivariate histograms of WT MEFs of NPC to face-versus-fiber distances showing lamin isoform-dependent 2D distribution patterns. Fig. S3 contains bivariate histograms of *Lmnb1*<sup>-/-</sup> and *Lmna*<sup>-/-</sup> MEFs. Fig. S4 presents violin plots comparing the number of NPCs detected in WT, *Lmna*<sup>-/-</sup>, *Lmnb1*<sup>-/-</sup>, and *Lmnb2*<sup>-/-</sup> MEFs. Fig. S5 presents Western blots of ELYS, NUP153, and TPR siRNA KD experiments and of anti-LC antibody specificity. Fig. S6 contains bivariate histograms of LA fiber–NPC and face center–NPC distances. Fig. S7 contains bivariate histograms of LC fiber–NPC and face center–NPC distances. Fig. S8 contains bivariate histograms of LB1 fiber–NPC and face center–NPC distances. Fig. S9 contains bivariate histograms of LB2 fiber–NPC and face center–NPC distances. Fig. S10 shows the effect of ELYS, NUP153, and TPR KD in *Lmnb1*<sup>-/-</sup> and *Lmna*<sup>-/-</sup> MEFs.

## Acknowledgments

The authors would like to acknowledge the Center for Advanced Microscopy and the Nikon Imaging Center at the Feinberg School of Medicine, Northwestern University, for assistance with imaging and the use of the Nikon Structured Illumination Microscope (N-SIM).

The N-SIM used in this study was purchased through the support of National Institutes of Health 1S10OD016342-01. The authors acknowledge the National Cancer Institute (T32CA080621 for M. Kittisopikul), Japan Society for the Promotion of Science (KAKENHI grant 19K21178 and KAKENHI grant 20K06617 for T. Shimi), Swiss National Science Foundation (grant SNSF 31003A\_179418 to O. Medalia), and the National Institute of General Medical Sciences (R35GM119619 to K. Jaqaman and R01GM106023 to Y. Zheng and R.D. Goldman).

The authors declare no competing financial interests.

Author contributions: M. Kittisopikul, T. Shimi, S.A. Adam, and R.D. Goldman conceived of the study. T. Shimi and M. Kittisopikul performed the light microscopy experiments. M. Tatli and O. Medalia analyzed cryo-electron tomography data. M. Kittisopikul and S.A. Adam ran the Western blots. J.R. Tran and Y. Zheng provided lamin null cell lines. M. Kittisopikul and K. Jaqaman performed the image and statistical analyses. M. Kittisopikul, T. Shimi, and M. Tatli prepared the figures. All authors contributed to the writing of the paper.

Submitted: 16 July 2020

Revised: 15 October 2020

Accepted: 5 January 2021

## References

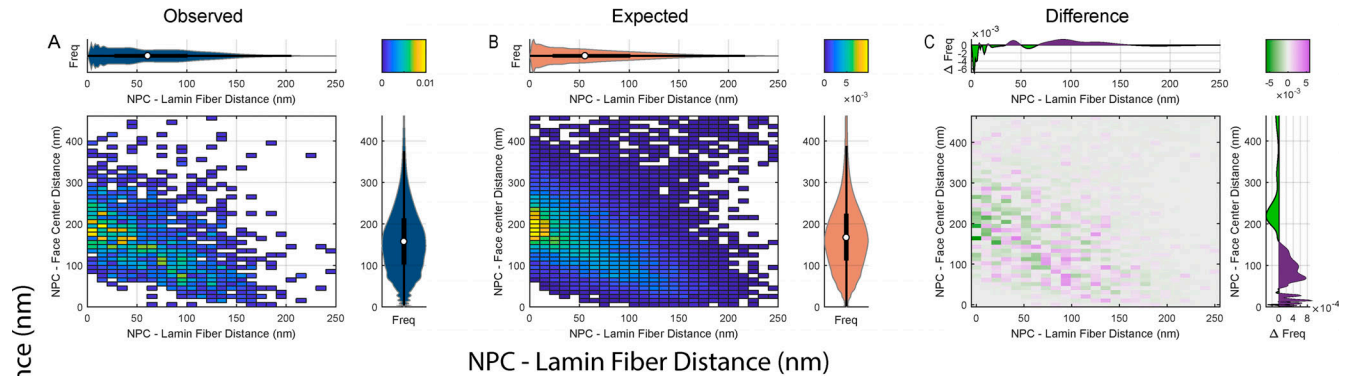
- Aebi, U., J. Cohn, L. Buhle, and L. Gerace. 1986. The nuclear lamina is a meshwork of intermediate-type filaments. *Nature*. 323:560–564. <https://doi.org/10.1038/323560a0>
- Al-Haboubi, T., D.K. Shumaker, J. Köser, M. Wehnert, and B. Fahrenkrog. 2011. Distinct association of the nuclear pore protein Nup153 with A- and B-type lamins. *Nucleus*. 2:500–509. <https://doi.org/10.4161/nucl.2.5.17913>
- Beck, M., and E. Hurt. 2017. The nuclear pore complex: understanding its function through structural insight. *Nat. Rev. Mol. Cell Biol.* 18:73–89. <https://doi.org/10.1038/nrm.2016.147>
- Broers, J.L., B.M. Machiels, G.J. van Eys, H.J. Kuijpers, E.M. Manders, R. van Driel, and F.C. Ramaekers. 1999. Dynamics of the nuclear lamina as monitored by GFP-tagged A-type lamins. *J. Cell Sci.* 112:3463–3475. <https://jcs.biologists.org/content/112/20/3463>
- Burke, B., and C.L. Stewart. 2014. Functional Architecture of the Cell's Nucleus in Development, Aging, and Disease. In *Current Topics in Developmental Biology*. Elsevier, San Diego. 1–52., <https://doi.org/10.1016/B978-0-12-397920-9.00006-8>
- Butin-Israeli, V. 2011. Simian virus 40 induces lamin A/C fluctuations and nuclear envelope deformation during cell entry. *Nucleus*. 2:320–330. <https://doi.org/10.4161/nucl.2.4.16371>
- Carrington, G., D. Tomlinson, and M. Peckham. 2019. Exploiting nanobodies and Aimers for superresolution imaging in light microscopy. *Mol. Biol. Cell*. 30:2737–2740. <https://doi.org/10.1091/mbc.E18-11-0694>
- Daigle, N., J. Beaudouin, L. Hartnell, G. Imreh, E. Hallberg, J. Lippincott-Schwartz, and J. Ellenberg. 2001. Nuclear pore complexes form immobile networks and have a very low turnover in live mammalian cells. *J. Cell Biol.* 154:71–84. <https://doi.org/10.1083/jcb.200101089>
- Dechat, T., T. Shimi, S.A. Adam, A.E. Rusinol, D.A. Andres, H.P. Spielmann, M.S. Sinensky, and R.D. Goldman. 2007. Alterations in mitosis and cell cycle progression caused by a mutant lamin A known to accelerate human aging. *Proc. Natl. Acad. Sci. USA*. 104:4955–4960. <https://doi.org/10.1073/pnas.0700854104>
- Doucet, C.M., J.A. Talamas, and M.W. Hetzer. 2010. Cell Cycle-Dependent Differences in Nuclear Pore Complex Assembly in Metazoa. *Cell*. 141:1030–1041. <https://doi.org/10.1016/j.cell.2010.04.036>
- Duheron, V., G. Chatel, U. Sauder, V. Oliveri, and B. Fahrenkrog. 2014. Structural characterization of altered nucleoporin Nup153 expression in human cells by thin-section electron microscopy. *Nucleus*. 5:601–612. <https://doi.org/10.4161/19491034.2014.990853>
- Dwyer, N., and G. Blobel. 1976. A modified procedure for the isolation of a pore complex-lamina fraction from rat liver nuclei. *J. Cell Biol.* 70:581–591. <https://doi.org/10.1083/jcb.70.3.581>
- Fawcett, D.W. 1966. On the occurrence of a fibrous lamina on the inner aspect of the nuclear envelope in certain cells of vertebrates. *Am. J. Anat.* 119:129–145. <https://doi.org/10.1002/aja.1001190108>
- Fišerová, J., M. Maniponová, T. Sieger, J. Uhlířová, L. Šebestová, M. Efenberková, M. Čapek, K. Fišer, and P. Hozák. 2019. Nuclear pore protein TPR associates with lamin B1 and affects nuclear lamina organization and nuclear pore distribution. *Cell. Mol. Life Sci.* 76:2199–2216. <https://doi.org/10.1007/s00018-019-03037-0>
- Fisher, D.Z., N. Chaudhary, and G. Blobel. 1986. cDNA sequencing of nuclear lamins A and C reveals primary and secondary structural homology to intermediate filament proteins. *Proc. Natl. Acad. Sci. USA*. 83:6450–6454. <https://doi.org/10.1073/pnas.83.17.6450>
- Franz, C., R. Walczak, S. Yavuz, R. Santarella, M. Gentzel, P. Askjaer, V. Galy, M. Hetzer, I.W. Mattaj, and W. Antonin. 2007. MEL-28/ELYS is required for the recruitment of nucleoporins to chromatin and post-mitotic nuclear pore complex assembly. *EMBO Rep.* 8:165–172. <https://doi.org/10.1038/sj.embor.7400889>
- Funasaka, T., E. Tsuka, and R.W. Wong. 2012. Regulation of autophagy by nucleoporin Tpr. *Sci. Rep.* 2:878. <https://doi.org/10.1038/srep00878>
- Galy, V., P. Askjaer, C. Franz, C. López-Iglesias, and I.W. Mattaj. 2006. MEL-28, a Novel Nuclear-Envelope and Kinetochore Protein Essential for Zygotic Nuclear-Envelope Assembly in *C. elegans*. *Curr. Biol.* 16:1748–1756. <https://doi.org/10.1016/j.cub.2006.06.067>
- Gerace, L., C. Comeau, and M. Benson. 1984. Organization and Modulation of Nuclear Lamina Structure. *J. Cell Sci.* 1(Supplement 1):137–160. [https://doi.org/10.1242/jcs.1984.Supplement\\_1.10](https://doi.org/10.1242/jcs.1984.Supplement_1.10)
- Goldman, A.E., G. Maul, P.M. Steinert, H.Y. Yang, and R.D. Goldman. 1986. Keratin-like proteins that coisolate with intermediate filaments of BHK-21 cells are nuclear lamins. *Proc. Natl. Acad. Sci. USA*. 83:3839–3843. <https://doi.org/10.1073/pnas.83.11.3839>

- Goldman, R.D., D.K. Shumaker, M.R. Erdos, M. Eriksson, A.E. Goldman, L.B. Gordon, Y. Gruenbaum, S. Khuon, M. Mendez, R. Varga, and F.S. Collins. 2004. Accumulation of mutant lamin A causes progressive changes in nuclear architecture in Hutchinson–Gilford progeria syndrome. *Proc. Natl. Acad. Sci. USA* 101:8963–8968. <https://doi.org/10.1073/pnas.0402943101>
- Gómez-Saldivar, G., A. Fernandez, Y. Hirano, M. Mauro, A. Lai, C. Ayuso, T. Haraguchi, Y. Hiraoka, F. Piano, and P. Askjaer. 2016. Identification of Conserved MEL-28/ELYS Domains with Essential Roles in Nuclear Assembly and Chromosome Segregation. *PLoS Genet.* 12:e1006131. <https://doi.org/10.1371/journal.pgen.1006131>
- Guelen, L., L. Pagie, E. Brasset, W. Meuleman, M.B. Faza, W. Talhout, B.H. Eussen, A. de Klein, L. Wessels, W. de Laat, and B. van Steensel. 2008. Domain organization of human chromosomes revealed by mapping of nuclear lamina interactions. *Nature*. 453:948–951. <https://doi.org/10.1038/nature06947>
- Guo, Y., and Y. Zheng. 2015. Lamins position the nuclear pores and centrosomes by modulating dynein. *Mol. Biol. Cell*. 26:3379–3389. <https://doi.org/10.1091/mbc.E15-07-0482>
- Guo, Y., Y. Kim, T. Shimi, R.D. Goldman, and Y. Zheng. 2014. Concentration-dependent lamin assembly and its roles in the localization of other nuclear proteins. *Mol. Biol. Cell*. 25:1287–1297. <https://doi.org/10.1091/mbc.e13-11-0644>
- Hase, M.E., and V.C. Cordes. 2003. Direct Interaction with Nup153 Mediates Binding of Tpr to the Periphery of the Nuclear Pore Complex. *Mol. Biol. Cell*. 14:1923–1940. <https://doi.org/10.1091/mbc.e02-09-0620>
- Ibarra, A., and M.W. Hetzer. 2015. Nuclear pore proteins and the control of genome functions. *Genes Dev.* 29:337–349. <https://doi.org/10.1101/gad.256495.114>
- Jevtić, P., A.C. Schibler, C.C. Wesley, G. Pegoraro, T. Misteli, and D.L. Levy. 2019. The nucleoporin ELYS regulates nuclear size by controlling NPC number and nuclear import capacity. *EMBO Rep.* 20. <https://doi.org/10.15252/embr.201847283>
- Kay, R.R., D. Fraser, and I.R. Johnston. 1972. A Method for the Rapid Isolation of Nuclear Membranes from Rat Liver. Characterisation of the Membrane Preparation and Its Associated DNA Polymerase. *Eur. J. Biochem.* 30:145–154. <https://doi.org/10.1111/j.1432-1033.1972.tb02081.x>
- Kittisopikul, M., L. Virtanen, P. Taimen, and R.D. Goldman. 2019. Quantitative Analysis of Nuclear Lamins Imaged by Super-Resolution Light Microscopy. *Cells*. 8:361. <https://doi.org/10.3390/cells8040361>
- Kittisopikul, M., A. Vahabikashi, T. Shimi, R.D. Goldman, and K. Jaqaman. 2020. Adaptive Multi-Orientation Resolution Analysis of Complex Filamentous Network Images. *Bioinformatics*. 36:5093–5103. <https://doi.org/10.1093/bioinformatics/btaa627>
- Kochin, V., T. Shimi, E. Torvaldson, S.A. Adam, A. Goldman, C.G. Pack, J. Melo-Cardenas, S.Y. Imanishi, R.D. Goldman, and J.E. Eriksson. 2014. Interphase phosphorylation of lamin A. *J. Cell Sci.* 127:2683–2696. <https://doi.org/10.1242/jcs.141820>
- Krull, S., J. Thyberg, B. Björkroth, H.R. Rackwitz, and V.C. Cordes. 2004. Nucleoporins as Components of the Nuclear Pore Complex Core Structure and Tpr as the Architectural Element of the Nuclear Basket. *Mol. Biol. Cell*. 15:4261–4277. <https://doi.org/10.1091/mbc.e04-03-0165>
- Krull, S., J. Dörries, B. Boysen, S. Reidenbach, L. Magnus, H. Norder, J. Thyberg, and V.C. Cordes. 2010. Protein Tpr is required for establishing nuclear pore-associated zones of heterochromatin exclusion. *EMBO J.* 29:1659–1673. <https://doi.org/10.1038/emboj.2010.54>
- Kuhn, T.M., and M. Capelson. 2019. Nuclear Pore Proteins in Regulation of Chromatin State. *Cells*. 8:1414. <https://doi.org/10.3390/cells8111414>
- Linkert, M., C.T. Rueden, C. Allan, J.M. Burel, W. Moore, A. Patterson, B. Loranger, J. Moore, C. Neves, D. MacDonald, et al. 2010. Metadata matters: access to image data in the real world. *J. Cell Biol.* 189:777–782. <https://doi.org/10.1083/jcb.201004104>
- Maeshima, K., K. Yahata, Y. Sasaki, R. Nakatomi, T. Tachibana, T. Hashikawa, F. Imamoto, and N. Imamoto. 2006. Cell-cycle-dependent dynamics of nuclear pores: pore-free islands and lamins. *J. Cell Sci.* 119:4442–4451. <https://doi.org/10.1242/jcs.03207>
- Mahamid, J., S. Pfeffer, M. Schaffer, E. Villa, R. Danev, L.K. Cuellar, F. Forster, A.A. Hyman, J.M. Plitzko, and W. Baumeister. 2016. Visualizing the molecular sociology at the HeLa cell nuclear periphery. *Science*. 351:969–972. <https://doi.org/10.1126/science.aad8857>
- Maul, G. 1977. Studies in ultrastructure. International review of cytology: Supplement; 6. Academic Press, New York.
- McCloskey, A., A. Ibarra, and M.W. Hetzer. 2018. Tpr regulates the total number of nuclear pore complexes per cell nucleus. *Genes Dev.* 32:1321–1331. <https://doi.org/10.1101/gad.315523.118>
- McKeon, F.D., M.W. Kirschner, and D. Caput. 1986. Homologies in both primary and secondary structure between nuclear envelope and intermediate filament proteins. *Nature*. 319:463–468. <https://doi.org/10.1038/319463a0>
- Mimura, Y., M. Takagi, M. Clever, and N. Imamoto. 2016. ELYS regulates the localization of LBR by modulating its phosphorylation state. *J. Cell Sci.* 129:4200–4212. <https://doi.org/10.1242/jcs.190678>
- Mimura, Y., S. Takemoto, T. Tachibana, Y. Ogawa, M. Nishimura, H. Yokota, and N. Imamoto. 2017. A statistical image analysis framework for pore-free islands derived from heterogeneity distribution of nuclear pore complexes. *Sci. Rep.* 7:16315. <https://doi.org/10.1038/s41598-017-16386-2>
- Moir, R.D., M. Yoon, S. Khuon, and R.D. Goldman. 2000. Nuclear Lamins a and B1. *J. Cell Biol.* 151:1155–1168. <https://doi.org/10.1083/jcb.151.6.1155>
- Mollan, K.R., I.M. Trumble, S. A. Reifeis, O. Ferrer, C.P. Bay, P.L. Baldoni, and M.G. Hudgens. 2020. Precise and accurate power of the rank-sum test for a continuous outcome. *Journal of Biopharmaceutical Statistics*. 30:639–648. <https://doi.org/10.1080/10543406.2020.1730866>
- Mounkes, L.C., S. Kozlov, L. Hernandez, T. Sullivan, and C.L. Stewart. 2003. A progeroid syndrome in mice is caused by defects in A-type lamins. *Nature*. 423:298–301. <https://doi.org/10.1038/nature01631>
- Nickell, S., F. Förster, A. Linaroudis, W.D. Net, F. Beck, R. Hegerl, W. Baumeister, and J.M. Plitzko. 2005. TOM software toolbox: acquisition and analysis for electron tomography. *J. Struct. Biol.* 149:227–234. <https://doi.org/10.1016/j.jsb.2004.10.006>
- Otsuka, S., and J. Ellenberg. 2018. Mechanisms of nuclear pore complex assembly – two different ways of building one molecular machine. *FEBS Lett.* 592:475–488. <https://doi.org/10.1002/1873-3468.12905>
- Ou, H.D., S. Phan, T.J. Deerinck, A. Thor, M.H. Ellisman, and C.C. O’Shea. 2017. ChromEMT: Visualizing 3D chromatin structure and compaction in interphase and mitotic cells. *Science*. 357:eaag0025. <https://doi.org/10.1126/science.aag0025>
- Peric-Hupkes, D., W. Meuleman, L. Pagie, S.W.M. Bruggeman, I. Solovei, W. Brugman, S. Gräf, P. Flicek, R.M. Kerkhoven, M. van Lohuizen, et al. 2010. Molecular Maps of the Reorganization of Genome-Nuclear Lamina Interactions during Differentiation. *Mol. Cell*. 38:603–613. <https://doi.org/10.1016/j.molcel.2010.03.016>
- Peters, R., J. Griedé, G.L. Burn, D.J. Williamson, and D.M. Owen. 2018. Quantitative fibre analysis of single-molecule localization microscopy data. *Sci. Rep.* 8:10418. <https://doi.org/10.1038/s41598-018-28691-5>
- R Core Team. 2020. R: A Language and Environment for Statistical Computing. R Foundation for Statistical Computing, Vienna, Austria. <https://www.R-project.org/> (accessed December 23, 2020).
- Rabut, G., V. Doye, and J. Ellenberg. 2004. Mapping the dynamic organization of the nuclear pore complex inside single living cells. *Nat. Cell Biol.* 6:1114–1121. <https://doi.org/10.1038/ncb1184>
- Raharjo, W.H., P. Enarson, T. Sullivan, C.L. Stewart, and B. Burke. 2001. Nuclear envelope defects associated with LMNA mutations cause dilated cardiomyopathy and Emery-Dreifuss muscular dystrophy. *J. Cell Sci.* 114:4447–4457.
- Rasala, B.A., A.V. Orjalo, Z. Shen, S. Briggs, and D.J. Forbes. 2006. ELYS is a dual nucleoporin/kinetochore protein required for nuclear pore assembly and proper cell division. *Proc. Natl. Acad. Sci. USA*. 103:17801–17806. <https://doi.org/10.1073/pnas.0608484103>
- Rasala, B.A., C. Ramos, A. Harel, and D.J. Forbes. 2008. Capture of AT-rich Chromatin by ELYS Recruits POM121 and NDC1 to Initiate Nuclear Pore Assembly. *Mol. Biol. Cell*. 19:3982–3996. <https://doi.org/10.1091/mbc.e08-01-0012>
- Roux, K.J., D.I. Kim, M. Raida, and B. Burke. 2012. A promiscuous biotin ligase fusion protein identifies proximal and interacting proteins in mammalian cells. *J. Cell Biol.* 196:801–810. <https://doi.org/10.1083/jcb.201112098>
- Scheer, U., J. Kartenbeck, M.F. Trendelenburg, J. Stadler, and W.W. Franke. 1976. Experimental disintegration of the nuclear envelope. Evidence for pore-connecting fibrils. *J. Cell Biol.* 69:1–18. <https://doi.org/10.1083/jcb.69.1.1>
- Shimi, T., and K. Pflieger. 2008. The A- and B-type nuclear lamin networks: microdomains involved in chromatin organization and transcription. *Genes Dev.* 22:3409–3421. <https://doi.org/10.1101/gad.1735208>
- Shimi, T., M. Kittisopikul, J. Tran, A.E. Goldman, S.A. Adam, Y. Zheng, K. Jaqaman, and R.D. Goldman. 2015. Structural organization of nuclear lamins A, C, B1, and B2 revealed by superresolution microscopy. *Mol. Biol. Cell*. 26:4075–4086. <https://doi.org/10.1091/mbc.E15-07-0461>
- Smythe, C., H.E. Jenkins, and C.J. Hutchison. 2000. Incorporation of the nuclear pore basket protein Nup153 into nuclear pore structures is dependent upon lamina assembly: evidence from cell-free extracts of *Xenopus* eggs. *EMBO J.* 19:3918–3931. <https://doi.org/10.1093/emboj/19.15.3918>

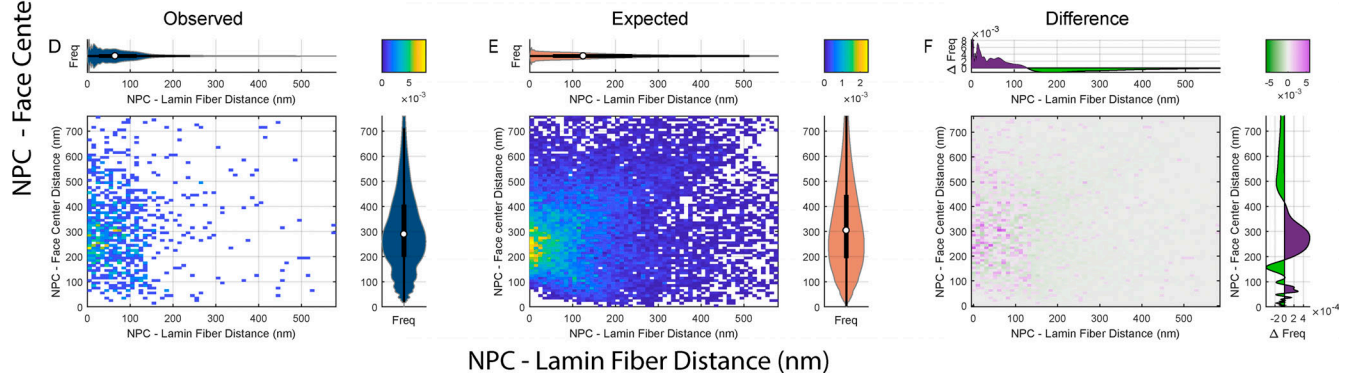
- Stelzer. 1998. Contrast, resolution, pixelation, dynamic range and signal-to-noise ratio: fundamental limits to resolution in fluorescence light microscopy. *Journal of Microscopy*. 189(1):15–24.
- Sullivan, T., D. Escalante-Alcalde, H. Bhatt, M. Anver, N. Bhat, K. Nagashima, C.L. Stewart, and B. Burke. 1999. Loss of a-Type Lamin Expression Compromises Nuclear Envelope Integrity Leading to Muscular Dystrophy. *J. Cell Biol.* 147:913–920. <https://doi.org/10.1083/jcb.147.5.913>
- Tatli, M., and O. Medalia. 2018. Insight into the functional organization of nuclear lamins in health and disease. *Curr. Opin. Cell Biol.* 54:72–79. <https://doi.org/10.1016/j.ceb.2018.05.001>
- Turgay, Y., M. Eibauer, A.E. Goldman, T. Shimi, M. Khayat, K. Ben-Harush, A. Dubrovsky-Gaup, K.T. Sapra, R.D. Goldman, and O. Medalia. 2017. The molecular architecture of lamins in somatic cells. *Nature*. 543:261–264. <https://doi.org/10.1038/nature21382>
- Unser, M. 1999. Splines: a perfect fit for signal and image processing. *IEEE Signal Process. Mag.* 16:22–38. <https://doi.org/10.1109/79.799930>
- Vollmer, B., M. Lorenz, D. Moreno-Andrés, M. Bodenhofer, P.D. Magistris, S.A. Astrinidis, A. Schooley, M. Flötenmeyer, S. Leptihn, and W. Antonin. 2015. Nup153 Recruits the Nup107-160 Complex to the Inner Nuclear Membrane for Interphasic Nuclear Pore Complex Assembly. *Dev. Cell.* 33:717–728. <https://doi.org/10.1016/j.devcel.2015.04.027>
- Walther, T.C. 2001. The nucleoporin Nup153 is required for nuclear pore basket formation, nuclear pore complex anchoring and import of a subset of nuclear proteins. *EMBO J.* 20:5703–5714. <https://doi.org/10.1093/emboj/20.20.5703>
- Xie, W., A. Chojnowski, T. Boudier, J.S.Y. Lim, S. Ahmed, Z. Ser, C. Stewart, and B. Burke. 2016. A-type Lamins Form Distinct Filamentous Networks with Differential Nuclear Pore Complex Associations. *Curr. Biol.* 26: 2651–2658. <https://doi.org/10.1016/j.cub.2016.07.049>

## Supplemental material

### WT MEF Lamin A - Single Nucleus



### *Lmnb1*<sup>-/-</sup> MEF Lamin A - Single Nucleus



G

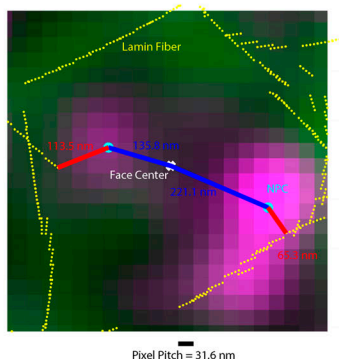


Figure S1. **Bivariate histograms of LA fiber–NPC and face center–NPC distances in single nuclei; illustration of distances.** (A) Observed bivariate histogram of NPC to LA face center distances versus NPC to LA fiber distances of a single WT MEF LA nucleus shown in Fig. 2 A. (B) Expected bivariate histogram of NPC to LA face center distances versus NPC to LA fiber distances of a single WT MEF nucleus under the null hypothesis. (C) Difference between the observed and expected distance distributions with purple indicating where the observed exceeds the expected frequency (Freq) and green showing when the observed frequency is less than the expected frequency. (D–F) Same as A–C except for the single *Lmnb1*<sup>-/-</sup> nucleus shown in Fig. 2 A. Marginal violin plots and box plots of the distances correspond with the half-violin plot counterparts of the same orientation and color as in Fig. 2 B. (G) Zoomed-in plot showing the NPC to LA fiber (red) and NPC to LA face center (blue) distances measured. Other colors correspond with those as in Fig. 2 B.

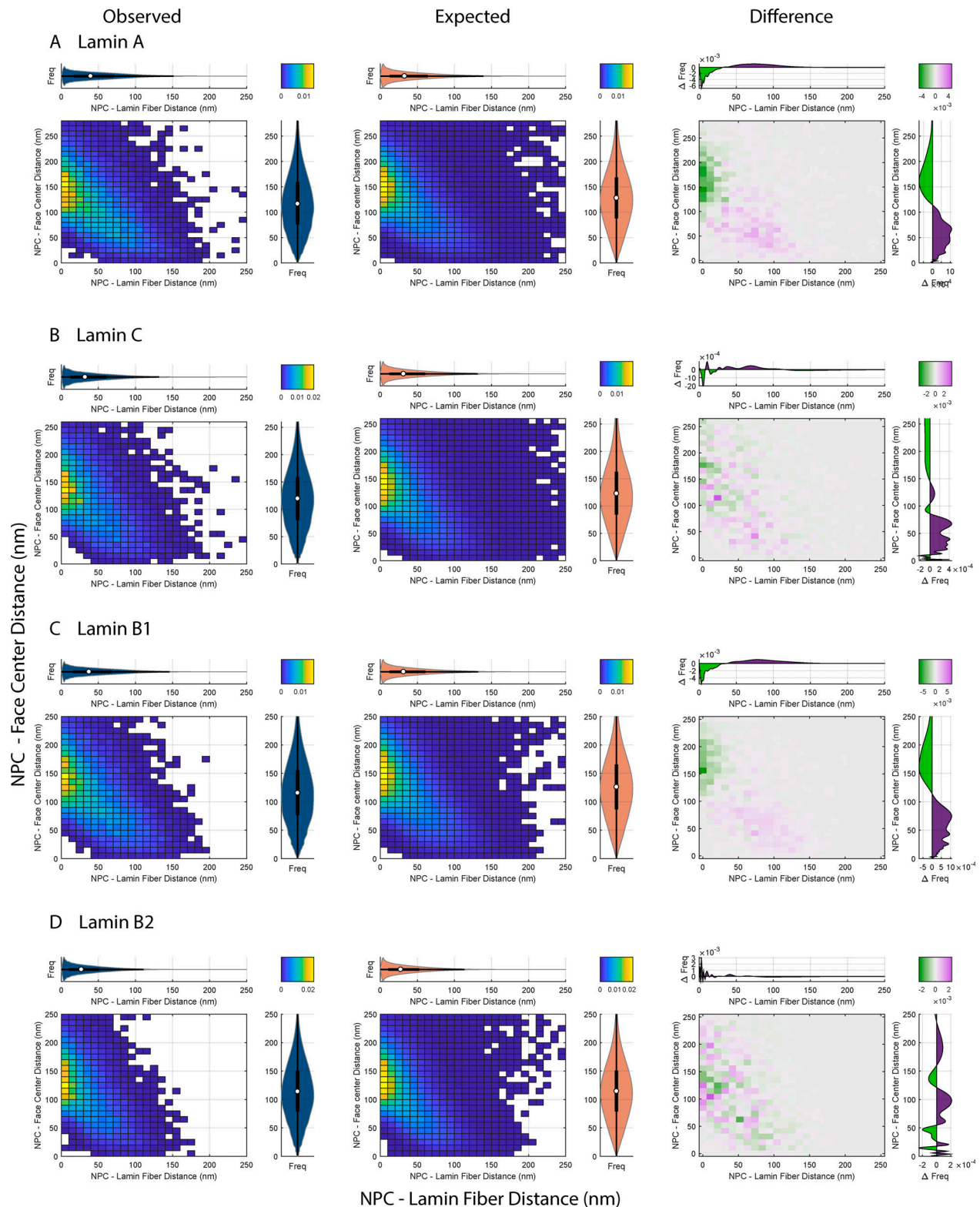


Figure S2. **Bivariate histograms of WT MEFs of NPC to face-versus-fiber distances show lamin isoform-dependent 2D distribution patterns.** (A) First row shows a bivariate distribution of NPC to LA fiber and face center distances in WT MEFs. (B) Second row shows bivariate distributions of NPC to LC fiber and face center distances. (C) Third row shows bivariate distributions of NPC to LB1 distances. (D) Fourth row shows bivariate distributions of NPC to LB2 distances. (A–D) First column represents the observed bivariate distribution. Second column represents the expected bivariate distribution. Third column represents the difference between expected and observed. Difference between the observed and expected distance distributions with purple indicating where the observed exceeds the expected frequency (Freq) and green showing when the observed frequency is less than the expected frequency. Marginal violin plots and box plots of the distances correspond with the half-violin plot counterparts of the same orientation and color as in Fig. 3 B. Each violin or box plot represents 10 cells with the number of NPCs detailed in Table 1.

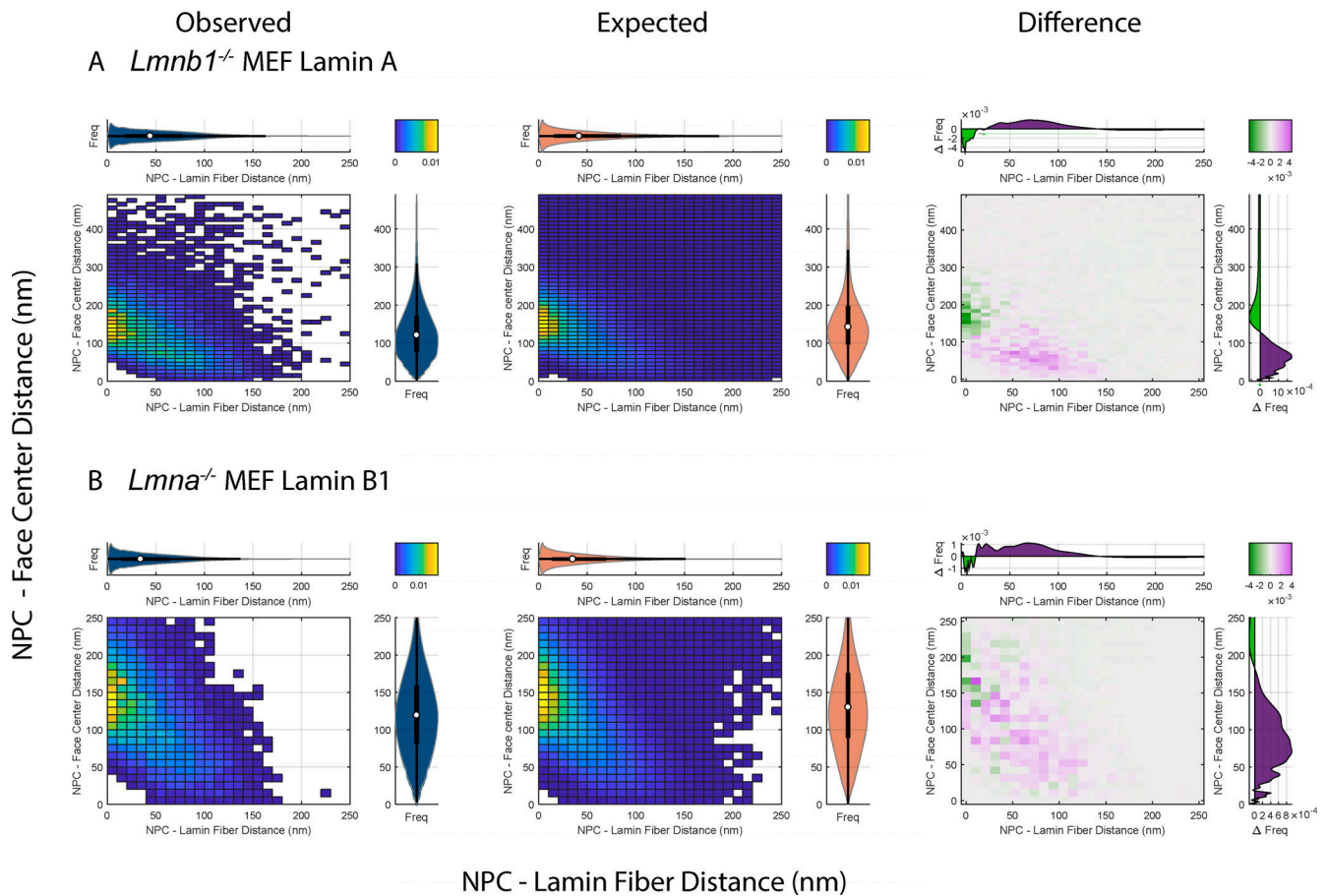


Figure S3. **Bivariate histograms of *Lmnb1*<sup>-/-</sup> and *Lmna*<sup>-/-</sup> MEFs.** (A) First row corresponds to the NPC to LA fiber and face center distances in *Lmnb1*<sup>-/-</sup> MEFs. (B) Second row shows NPC to LB1 fiber and face center distances in *Lmna*<sup>-/-</sup> MEFs. Columns are as in Fig. S2. Each violin or box plot represents 10 cells with the number of NPCs detailed in Table 1. Freq, frequency.

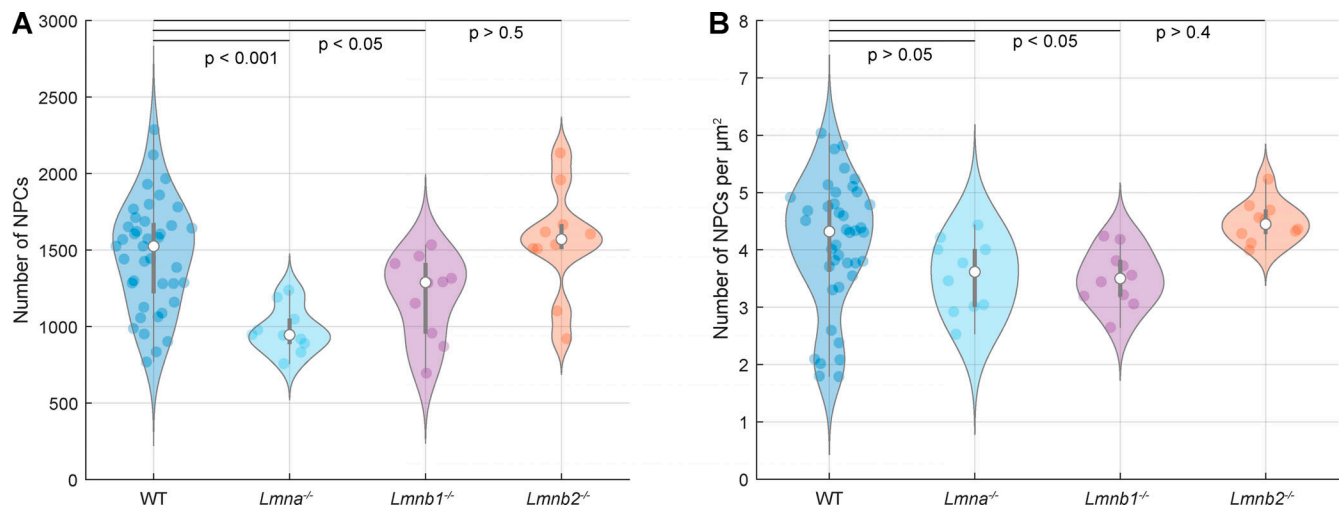
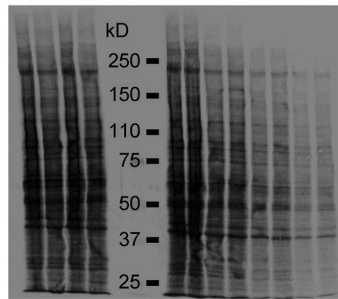


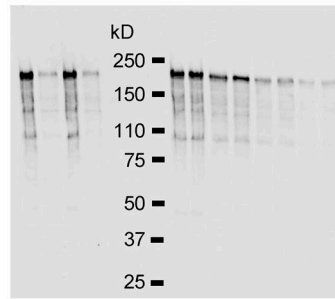
Figure S4. **Violin plots comparing the number of NPCs detected in WT, *Lmna*<sup>-/-</sup>, *Lmnb1*<sup>-/-</sup>, and *Lmnb2*<sup>-/-</sup> MEFs.** (A and B) Number of NPCs per nucleus (A) and NPC density for WT, *Lmna*<sup>-/-</sup>, *Lmnb1*<sup>-/-</sup>, and *Lmnb2*<sup>-/-</sup> MEFs (B). The WT category is comprised of 10 cells pooled from the cells counted in the first four rows of Table 1 and Table 2, consisting of cells of WT genotype and stained with antibodies against the four lamin isoforms. The *Lmna*<sup>-/-</sup> category consists of 10 cells corresponding to the sixth row of Table 1 and Table 2. The *Lmnb1*<sup>-/-</sup> category consists of 10 cells corresponding to the fifth row of Table 1 and Table 2. The *Lmnb2*<sup>-/-</sup> category consists of 10 cells. The white circles indicate the medians. The thick gray bar indicates the interquartile range (IQR). The gray whiskers indicate 1.5 times the IQR. Each colored circle corresponds to a single cell. The Mann-Whitney *U* test was used to compare distributions and determine P values as described in the Materials and methods.

### A NUP153 KD 75-90%

WT WT WT Total Protein Load %  
KD KD 100 50 25 10

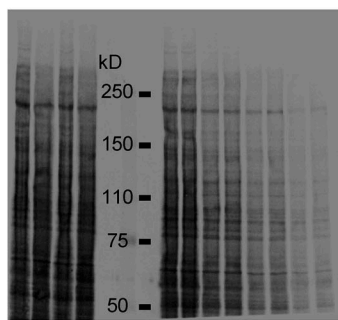


WT WT WT Total Protein Load %  
KD KD 100 50 25 10

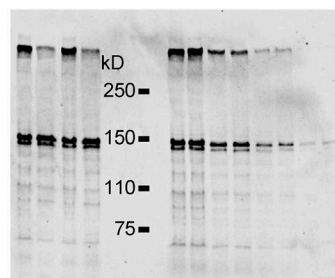


### B ELYS KD 50 - 60%

WT WT WT Total Protein Load %  
KD KD 100 50 25 10

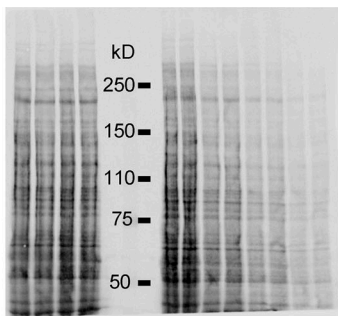


WT WT WT Total Protein Load %  
KD KD 100 50 25 10



### C TPR KD ~40%

WT WT WT Total Protein Load %  
KD KD 100 50 25 10



WT WT WT Total Protein Load %  
KD KD 100 50 25 10

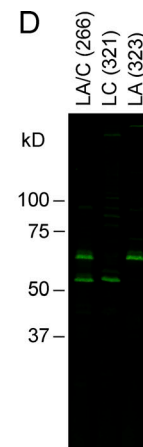
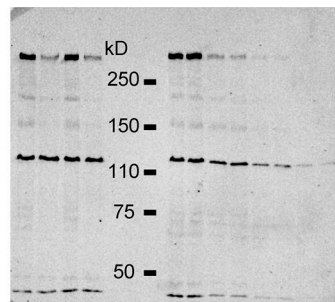


Figure S5. **Western blots of ELYS, NUP153, and TPR siRNA KD experiments and of anti-LC specificity.** (A–C) siRNA KDs were performed and quantified as described in Materials and methods. The panels on the left are the total protein stains of the immunoblots with each sample loaded in duplicate. The panels on the right are the immunoblots for each antibody NUP153 (A), ELYS (B), and TPR (C). The degree of KD for each protein was determined by quantifying the average intensity of each duplicate after correction for protein load and comparison to the dilution series of the total protein load from WT cells. (D) Whole cell lysates of WT MEFs in Laemmli sample buffer were resolved by SDS-PAGE ( $6 \times 10^4$  cells/lane); immunoblotted by anti-LA/LC (266) 1:1,000; anti-LC (321) 1:500; and anti-LA (323) 1:1,000 primary antibodies along with anti-rabbit secondary antibody (LICOR; IRDye 800CW) and visualized using Odyssey Fc at 800 nm.

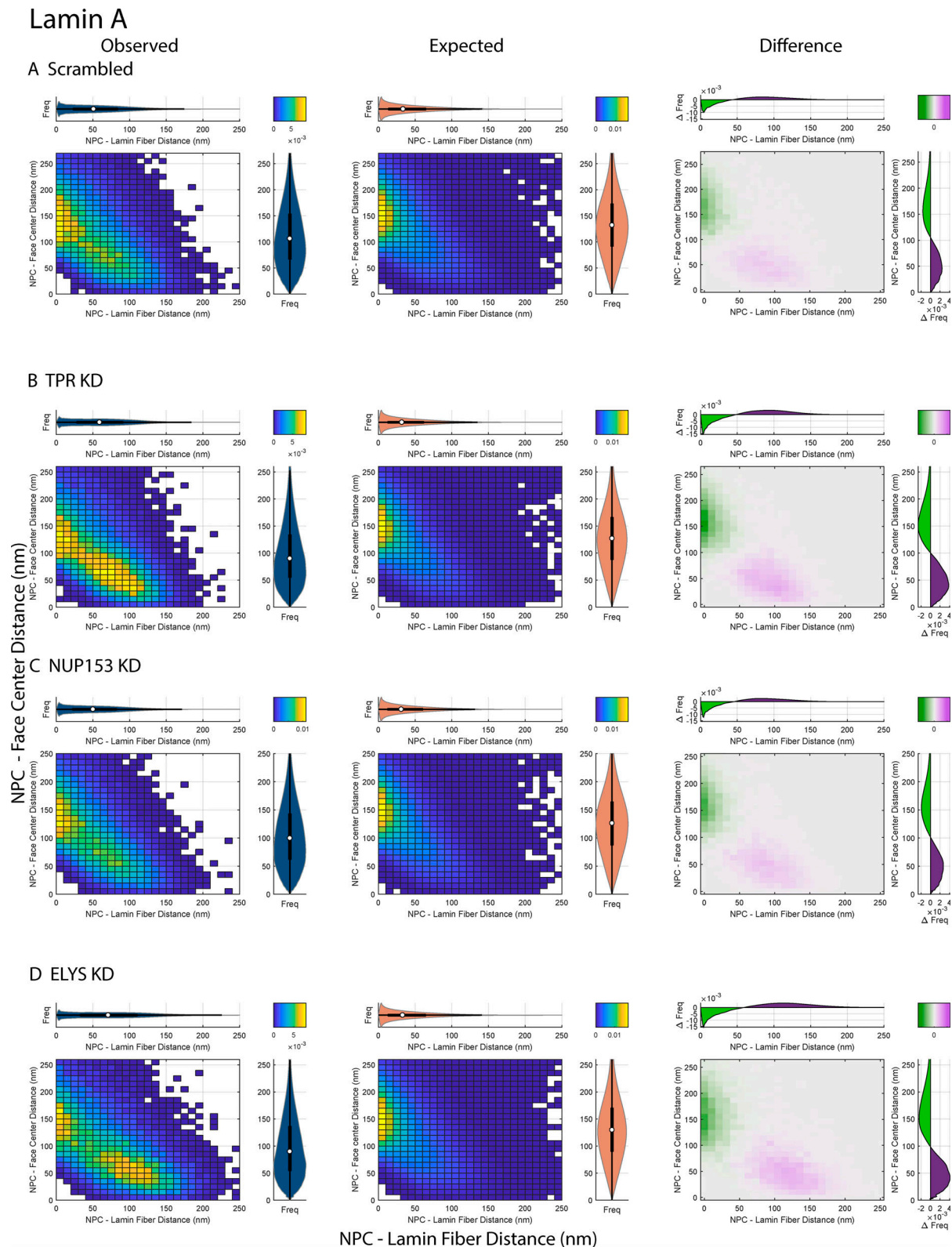


Figure S6. **Bivariate histograms of LA fiber–NPC and face center–NPC distances.** (A) First row shows a bivariate distribution of NPC to LA fiber and face center distances in WT MEFs after treatment with scramble siRNA. (B) Second row shows the same with siRNA KD of TPR. (C) Third row shows the same with siRNA KD of NUP153. (D) Fourth row shows the same with siRNA KD of ELYS. (A–D) First column represents the observed bivariate distribution. Second column represents the expected distance distributions with purple indicating where the observed exceeds the expected frequency (Freq) and green showing when the observed frequency is less than the expected frequency. Marginal violin plots and box plots of the distances correspond with the half-violin plot counterparts of the same orientation and color as in Fig. 5, B–E. Each violin or box plot represents 20 cells with the number of NPCs detailed in Table 3.

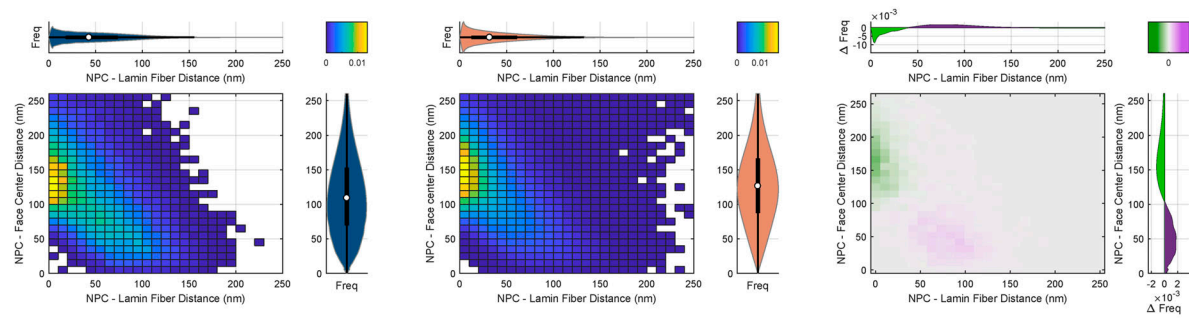
# Lamin C

Observed

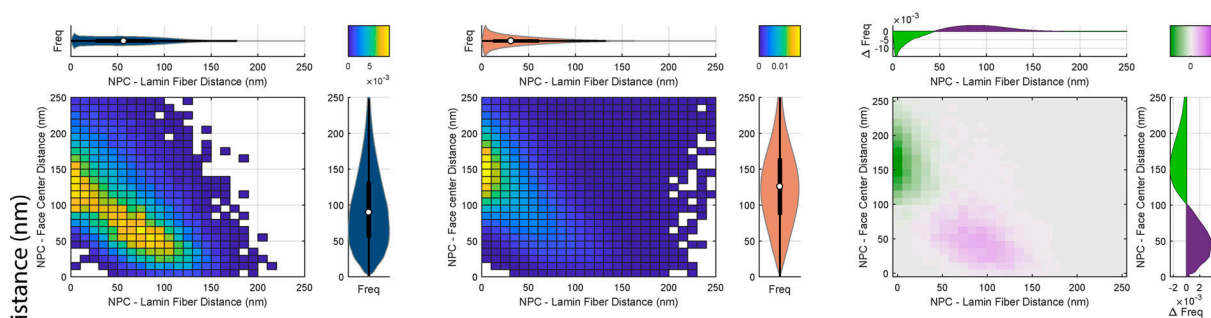
Expected

Difference

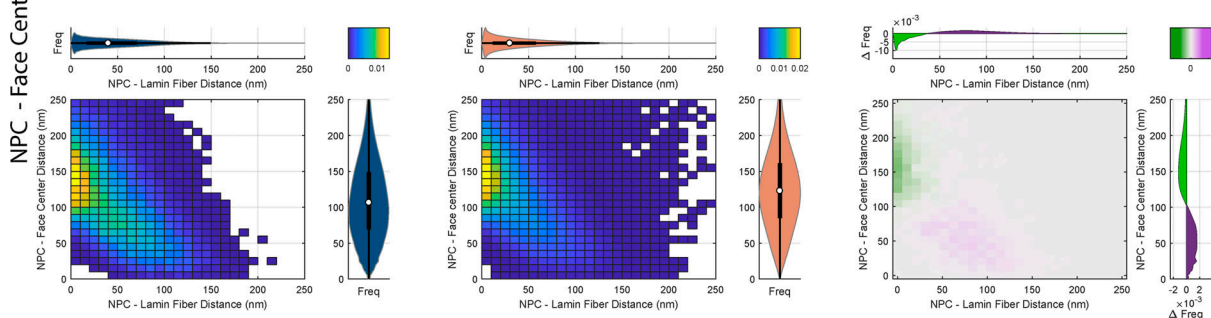
A Scrambled



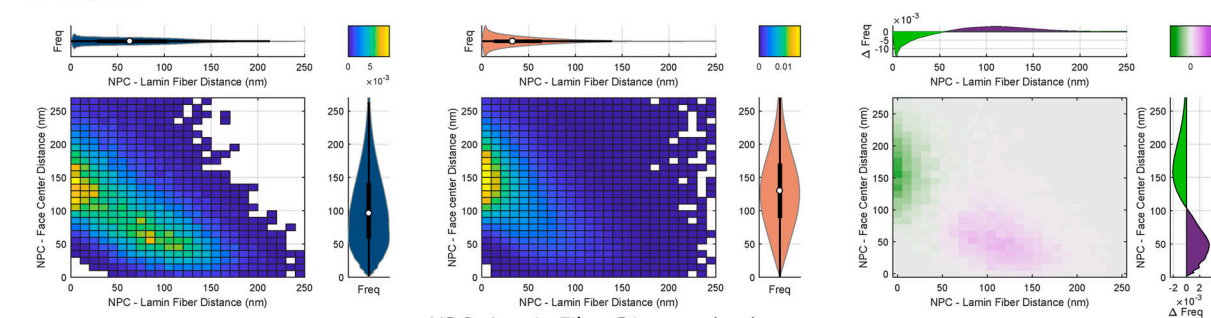
B TPR KD



C NUP153 KD



D ELYS KD



NPC - Lamin Fiber Distance (nm)

Figure S7. **Bivariate histograms of LC fiber–NPC and face center–NPC distances.** (A) First row shows a bivariate distribution of NPC to LC fiber and face center distances in WT MEFs after treatment with scramble siRNA. (B) Second row shows the same with siRNA KD of TPR. (C) Third row shows the same with siRNA KD of NUP153. (D) Fourth row shows the same with siRNA KD of ELYS. (A–D) First column represents the observed bivariate distribution. Second column represents the expected distance distribution. Third column represents the difference between expected and observed. Difference between the observed and expected distance distributions with purple indicating where the observed exceeds the expected frequency and green showing when the observed frequency (Freq) is less than the expected frequency. Marginal violin plots and box plots of the distances correspond with the half-violin plot counterparts of the same orientation and color as in Fig. 6, B–E. Each violin or box plot represents 20 cells with the number of NPCs detailed in Table 3.



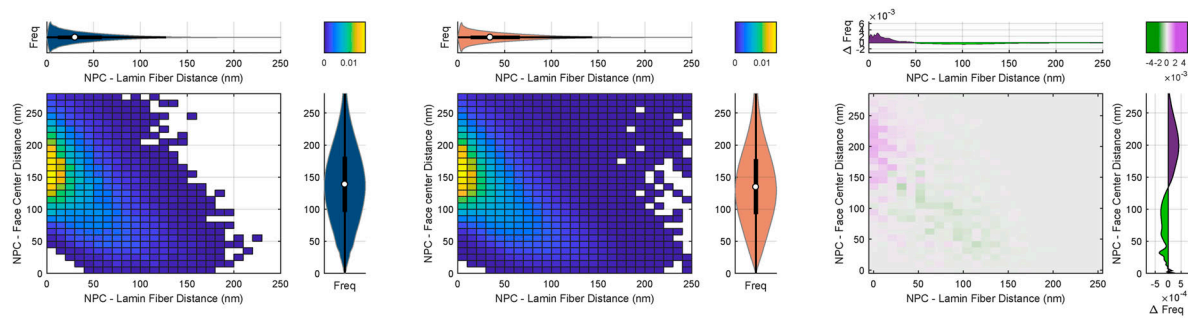
## Lamin B2

Observed

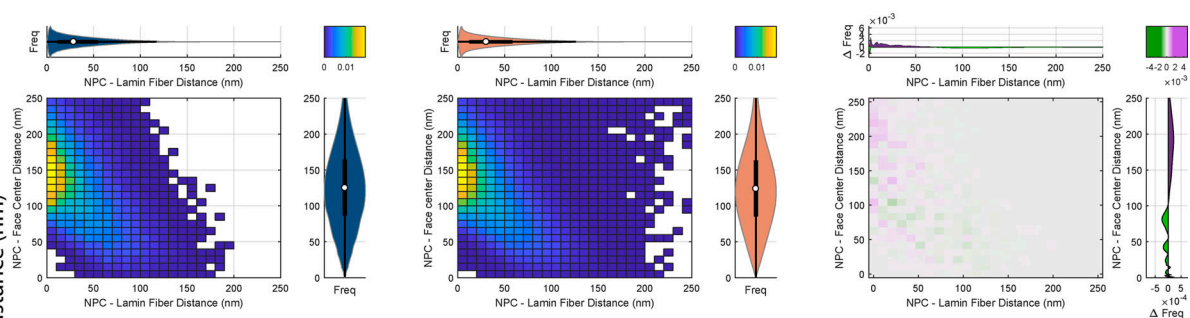
Expected

Difference

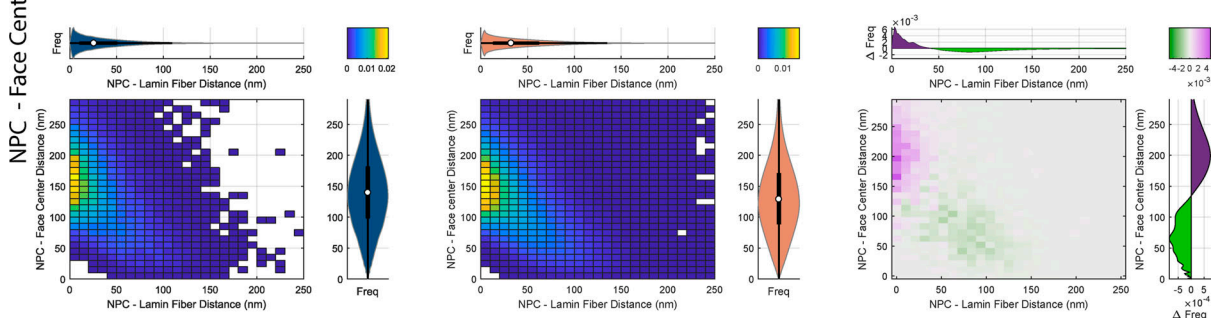
A Scrambled



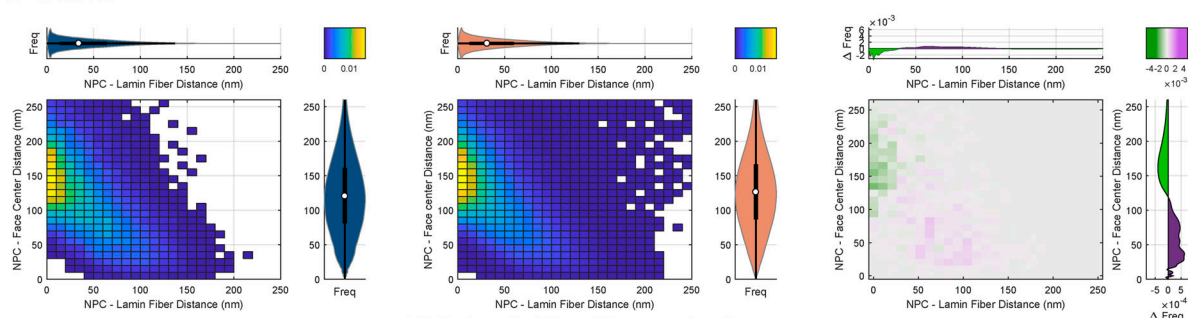
B TPR KD



C NUP153 KD



D ELYS KD



NPC - Lamin Fiber Distance (nm)

Figure S9. **Bivariate histograms of LB2 fiber–NPC and face center–NPC distances.** (A) First row shows a bivariate distribution of NPC to LB2 fiber and face center distances in WT MEFs after treatment with scramble siRNA. (B) Second row shows the same with siRNA KD of TPR. (C) Third row shows the same with siRNA KD of NUP153. (D) Fourth row shows the same with siRNA KD of ELYS. (A–D) First column represents the observed bivariate distribution. Second column represents the expected distance distribution. Third column represents the difference between expected and observed. Difference between the observed and expected distance distributions with purple indicating where the observed exceeds the expected frequency and green showing when the observed frequency is less than the expected frequency. Marginal violin plots and box plots of the distances correspond with the half-violin plot counterparts of the same orientation and color as in panels B–E of Fig. 8. Each violin or box plot represents 20 cells with the number of NPCs detailed in Table 3.

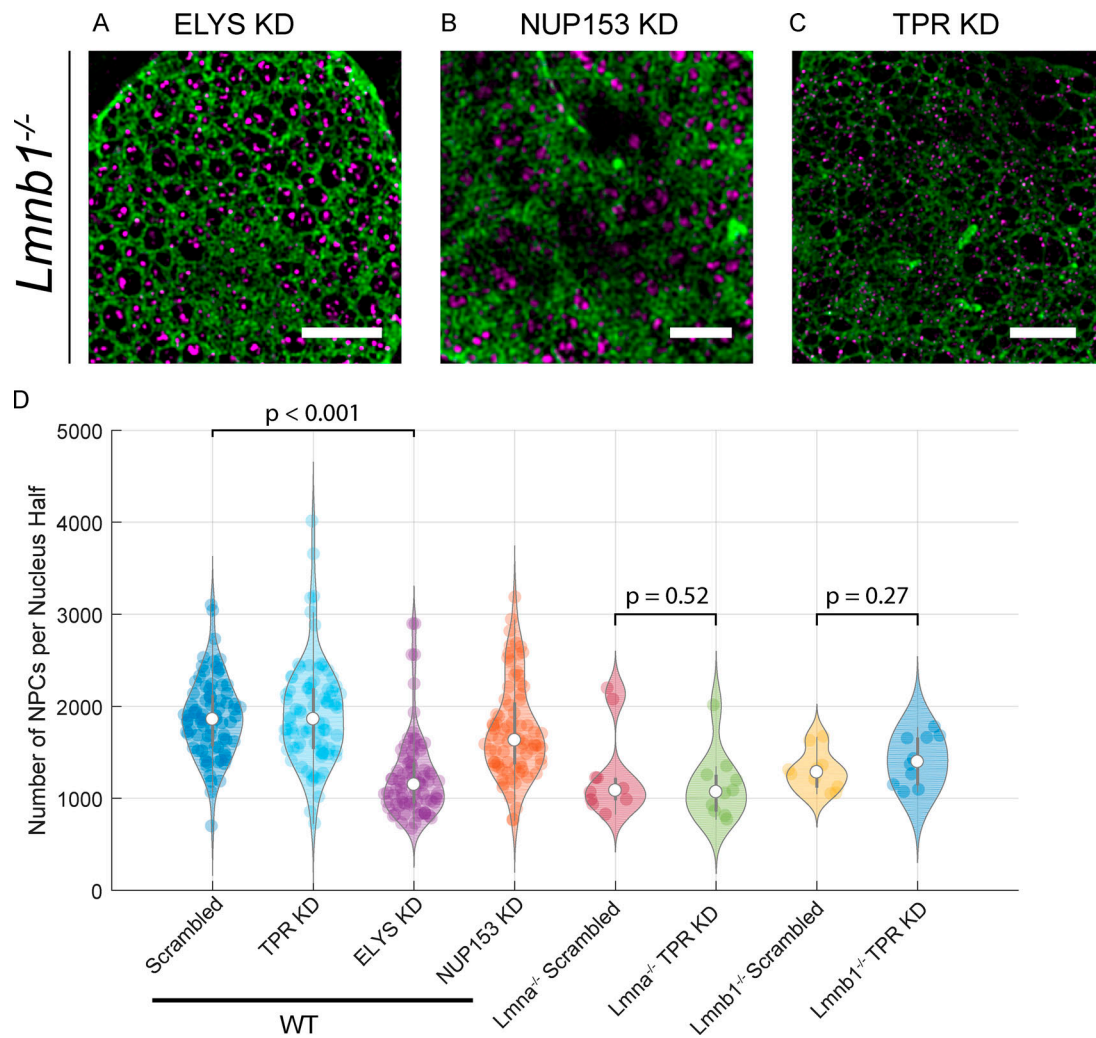


Figure S10. **Effect of ELYS, NUP153, and TPR KD in *Lmnb1*<sup>-/-</sup> and *Lmna*<sup>-/-</sup> MEFs.** (A–C) Immunofluorescence images of *Lmnb1*<sup>-/-</sup> MEFs ELYS KD (A), NUP153 KD (B), TPR KD (C) with LA (green) and NPCs (magenta) labeled. (D) Number of NPCs per MEF nuclei in a single focal plane in WT MEFs after ELYS (80 cells), NUP153 (80 cells), and TPR (80 cells) KD; in *Lmna*<sup>-/-</sup> MEFs after TPR KD (10 cells); and in *Lmnb1*<sup>-/-</sup> MEFs after TPR KD (10 cells) in comparison to scrambled siRNA (80 WT MEFs, 10 *Lmna*<sup>-/-</sup> MEFs, 10 *Lmnb1*<sup>-/-</sup> MEFs). The white circles indicate the medians. The thick gray bar indicates the interquartile range (IQR). The gray whiskers indicate 1.5 times the IQR. Each colored circle represents a single cell. The Mann-Whitney *U* test was used to compare the distributions as described in the Materials and methods. Scale bar = 10  $\mu$ m.